ADVANCED FUNCTIONAL MATERIALS
www.afm-journal.de

Performance Optimization of Parallel-Like Ternary Organic Solar Cells through Simultaneous Improvement in Charge Generation and Transport

Wisnu Tantyo Hadmojo, Febrian Tri Adhi Wibowo, Wooseop Lee, Hye-Kyung Jang, Yeongsik Kim, Septy Sinaga, Minsuk Park, Sang-Yong Ju, Du Yeol Ryu, In Hwan Jung,* and Sung-Yeon Jang**

Ternary organic photovoltaic (OPV) devices with multiple light-absorbing active materials have emerged as an efficient strategy for realizing further improvements in the power conversion efficiency (PCE) without building complex multijunction structures. However, the third component often acts as recombination centers and, hence, the optimization of ternary blend morphology poses a major challenge to improving the PCE of these devices. In this work, the performance of OPVs is enhanced through the morphological modification of nonfullerene acceptor (NFA)-containing binary active layers. This modification is achieved by incorporating fullerenes into the layers. The uniformly dispersed fullerenes are sufficiently continuous and successfully mediate the ordering of NFA without charge or energy transfer. Owing to the simultaneous improvement in the charge generation and extraction, the PCE (12.1%) of these parallel-linked ternary devices is considerably higher than those of the corresponding binary devices (9.95% and 7.78%). Moreover, the additional energy loss of the ternary device is minimized, compared with that of the NFA-based binary device, due to the judicious control of the effective donor:acceptor composition of the ternary blends.

1. Introduction

Recent development in low-bandgap organic nonfullerene acceptors (NFAs) and high-bandgap donor polymers has effectively extended the light utilization of organic photovoltaic (OPV) devices.[1–3] In particular, due to the photon-to-current conversion up to the near-infrared (NIR) region, a power conversion efficiency (PCE) of 9–12% has been achieved for the OPV devices using indacenodithiophene-based small molecule NFAs such as ITIC.[4–7] However, the morphological characteristics of NFA-based bulk heterojunction (BHJ) active films differ from those of conventional fullerene-based BHJ films. The corresponding suboptimal charge generation and transport have often resulted in NFA-based BHJ active layers. Efficient morphological manipulation of these layers may provide the opportunity for further improvement in the performance of these devices.

Construction of ternary BHJ layers with multiple light-absorbing active materials has emerged as an efficient strategy for improving the PCE of OPV devices without building complex multijunction structures (i.e., tandem devices).[8–13] The choice of the third component with appropriate energy levels and complementary absorption is crucial for optimizing the current density (J_{SC}) and open-circuit voltage (V_{OC}) of the devices.[14–19] However, the effect of this component on the morphology (as manifested through the occurrence of recombination centers) may be unfavorable for charge generation and/or charge transport.[20–22] Optimization of the ternary blend (including NFA) morphology for maximum charge generation/transport and minimum energy loss represents a major challenge to the improvement of PCE devices.

The use of fullerenes as the third component for the NFA-containing BHJ blends has often improved the device performance due to the enhanced visible absorption by the fullerenes or the charge cascading effects from NFAs to these fullerenes.[10,23,24] While some fullerenes exhibited efficient absorption at ≈400–500 nm, the charge transfer from higher-lying lowest unoccupied molecular orbital (LUMO) levels of NFAs to lower-lying LUMO levels of fullerenes enhanced electron transport.[23] However, the mismatch of the LUMO levels of the fullerenes and NFA increased the energy loss of the devices

W. T. Hadmojo, F. T. A. Wibowo, S. Sinaga, Prof. I. H. Jung, Prof. S.-Y. Jang
Department of Chemistry
Kookmin University
77 Jeongneung-ro, Seongbuk-gu, Seoul 02707, Republic of Korea
E-mail: ihjung@kookmin.ac.kr; syjang@kookmin.ac.kr
W. Lee, H.-K. Jang, Y. Kim, Prof. D. Y. Ryu
Department of Chemical and Biomolecular Engineering
Yonsei University
50 Yonsei-ro, Seodaemun-gu, Seoul 03722, Republic of Korea
E-mail: dyryu@yonsei.ac.kr
M. Park, Prof. S.-Y. Ju
Department of Chemistry
Yonsei University
50 Yonsei-ro, Seodaemun-gu, Seoul 03722, Republic of Korea
The ORCID identification number(s) for the author(s) of this article can be found under https://doi.org/10.1002/adfm.201808731.

DOI: 10.1002/adfm.201808731

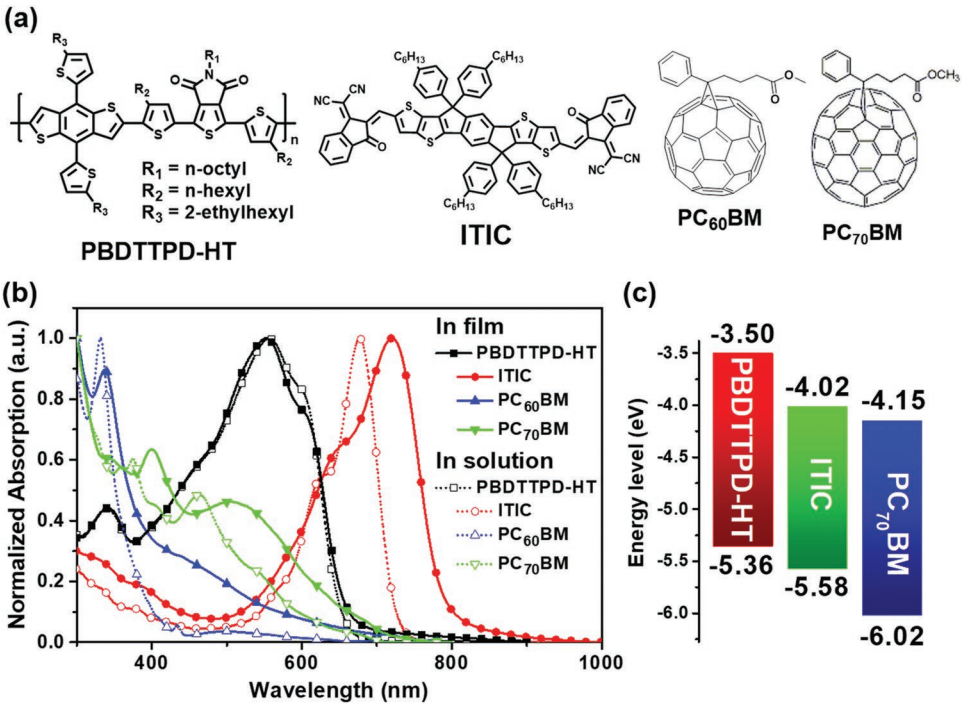

Figure 1. a) Chemical structure of PBDTTPD-HT, ITIC, and fullerenes ($PC_{70}BM$ and $PC_{60}BM$), b) Ultraviolet–visible (UV–vis) absorption in solution and films, and c) energy diagram of the PBDTTPD-HT, ITIC, and $PC_{70}BM$.

(defined as E_{loss} = bandgap $-qV_{OC}$, where q is the elementary charge). This resulted in a considerably lower V_{OC} of the ternary devices compared with that of binary NFA-based devices.[23,24]

Herein, we achieved enhanced performance of OPV devices via morphological modification induced by fullerene incorporation into the NFA-based binary active layers. The ternary BHJ active layers contained a wide-bandgap donor polymer (PBDTTPD-HT) and ITIC/fullerene binary acceptors. The incorporated fullerenes ($PC_{70}BM$ and $PC_{60}BM$) served as the mediator that enhanced the ordering of ITIC, and the fine aggregates of these fullerenes were uniformly dispersed with sufficient continuity. As a result, the charge generation and extraction of the ternary devices were significantly higher than those of the binary devices. No energy or charge transfer between NFA and fullerenes occurred, indicating that the ternary devices operate in accordance with a parallel-like device model. The performance of parallel-like ternary OPVs was tunable with respect to the weight fraction of NFA and fullerenes. In addition, the optimized PCEs of the ternary devices (12.09% and 11.96%) were substantially higher than those of the binary devices (9.95% and 7.78%). Moreover, the additional energy loss of the ternary devices, compared with that of the NFA-based binary device, was minimized, owing to the judiciously adjusted composition of the ternary blends.

2. Results and Discussion

2.1. Performance of Ternary Devices

The chemical structures of the donor polymer (PBDTTPD-HT), an NFA (ITIC), and fullerene acceptors ($PC_{70}BM$ and $PC_{60}BM$) used in this study are shown in **Figure 1**a. PBDTTPD-HT was chosen as an electron donor because it has complementary absorption with the acceptors (fullerenes and ITIC). In addition, the low energy loss (0.59 eV) was achievable by using ITIC.[25] The optical bandgap (E_g) of amorphous PBDTTPD-HT was 1.88 eV (Figure 1b,c).[25] The ITIC (bandgap = 1.56 eV) was selected as the NFA owing to its complementary absorption and appropriate energy levels with respect to those of PBDTTPD-HT. The energy level diagram, determined via cyclic voltammetry (Figure S1, Supporting Information), confirms sufficient driving force for charge separation at the PBDTTPD-HT/ITIC and PBDTTPD-HT/$PC_{70}BM$ interfaces. **Figure 2**b–d and Figures S2–S6 (Supporting Information) show the current density–voltage (J–V) characteristics and external quantum efficiency (EQE) spectra of the inverted-structure OPV devices (binary and ternary). The PCE (9.95%) of the PBDTTPD-HT:ITIC binary device (V_{OC}: 0.97 V; J_{SC}: 14.86 mA cm^{-2}; fill factor (FF): 0.69) was higher than that (7.78%) of the PBDTTPD-HT:$PC_{70}BM$ binary device (V_{OC}: 0.86 V; J_{SC}: 12.09 mA cm^{-2}; FF: 0.75). The ratio of PBDTTPD-HT:$PC_{70}BM$ and PBDTTPD-HT:ITIC was 1:1.5 w/w. The extended absorption ITIC yielded substantially higher J_{SC} than that of the PBDTTPD-HT:$PC_{70}BM$ devices (Figures S2 and S4, Supporting Information), which exhibited limited use of the solar spectrum. Furthermore, the V_{OC} value increased owing to the high-lying LUMO energy level of ITIC (Figures S2 and S4, Supporting Information). However, the considerably lower FF of the PBDTTPD-HT:ITIC device compared with that of the PBDTTPD-HT:$PC_{70}BM$ devices (0.69 vs 0.75) was attributable to lower electron mobility and/or suboptimal morphology. The performance of the binary devices at various donor:acceptor ratios is summarized in Figures S2–S4 and Tables S1–S3 (Supporting Information).

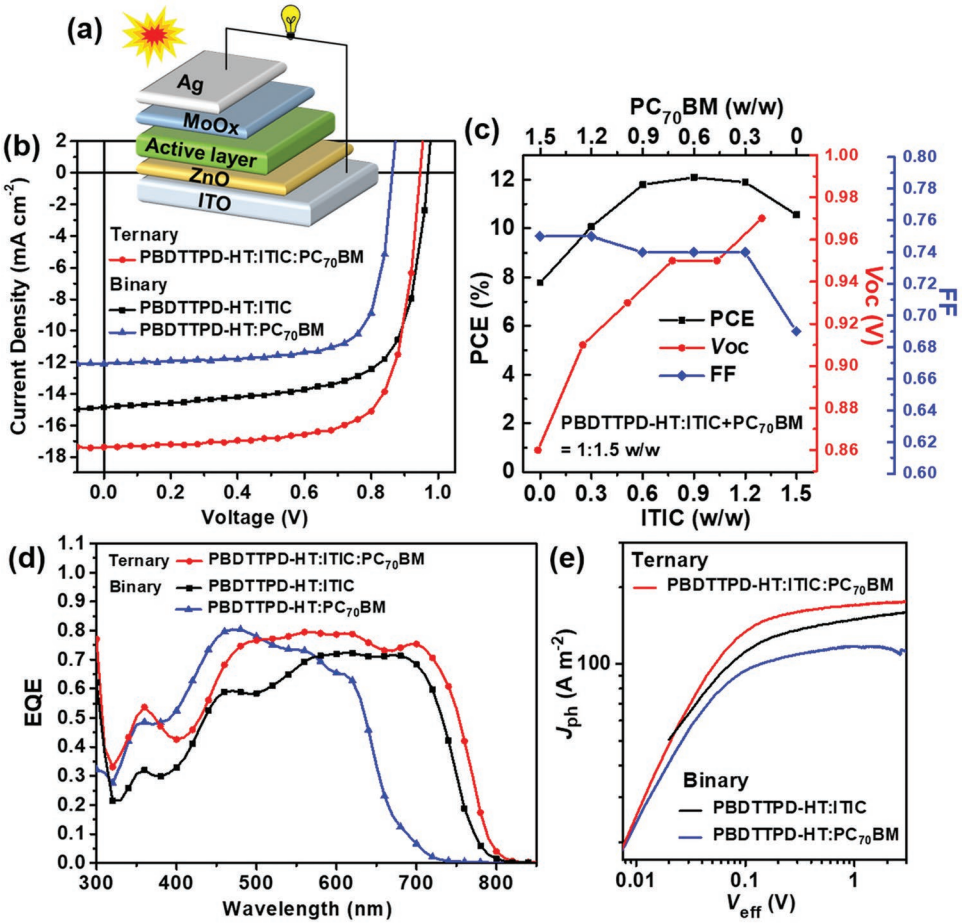

Figure 2. a) Architecture of an inverted OPV device, b) J–V characteristics of the ternary devices (PBDTTPD-HT:ITIC:$PC_{70}BM$ = 1:0.9:0.6 w/w) and binary devices (PBDTTPD-HT:ITIC = 1:1.5 w/w and PBDTTPD-HT:$PC_{70}BM$ = 1:1.5 w/w), c) composition dependence of PCE, V_{OC}, and FF associated with the ternary devices, corresponding d) EQE spectra, and e) J_{ph}–V_{eff} characteristics of the respective ternary and binary devices.

Ternary OPV devices exhibited significant improvements in performance. A PCE of 12.09% (V_{OC}: 0.95 V; J_{SC}: 17.38 mA cm^{-2}; and FF: 0.74) was realized for the PBDTTPD-HT:ITIC:$PC_{70}BM$ ternary device. A donor:acceptor (i.e., PBDTTPD-HT:ITIC + $PC_{70}BM$) weight ratio of 1:1.5 w/w was employed for the ternary devices studied. The device performance was strongly influenced by the fractions of NFA and fullerenes in the ternary active layers, and an optimum PCE was obtained at an ITIC:$PC_{70}BM$ ratio of 0.9:0.6 w/w (Figure 2c and **Table 1**). The J_{SC} of the ternary device (17.38 mA cm^{-2}) was substantially higher than those of the binary devices (12.09 and 14.86 mA cm^{-2}). Similarly, the EQE response of the ternary device was considerably higher than that of the PBDTTPD-HT:ITIC binary device, especially in the near-infrared region (Figure 2d), where $PC_{70}BM$ exhibits negligible absorption. This result, although surprising (since ≈40% less ITIC was incorporated into the ternary device than in the binary device), indicated that the addition of $PC_{70}BM$ was beneficial for the charge collection efficiency in ternary devices. The FF of the ternary device (0.74) was significantly higher than that of the PBDTTPD-HT:ITIC binary device (0.69) owing to $PC_{70}BM$ incorporation. Notably, the corresponding V_{OC} was marginally lower than that of the binary device, indicating that the energy loss associated with this incorporation was minimal. The binary and ternary devices containing $PC_{60}BM$ as the fullerene acceptor exhibited identical characteristics to those of the devices containing $PC_{70}BM$ (Figure S6 and Table S5, Supporting Information).

2.2. Charge Generation and Collection Properties

The effects of fullerenes on the charge transport properties of the ternary blends were investigated by measuring, via space charge–limited current (SCLC) analysis (Figures S9 and S10, Supporting Information). Hole- or electron-only devices were fabricated using ITO/PEDOT:PSS/active layer/MoO_x/Ag or ITO/ZnO/active layer/ZnO/Al configurations, respectively. The hole mobility (μ_h) and electron mobility (μ_e), as determined from the Mott–Gurney law in a steady-state SCLC trap-free regime, are listed in Table S6 (Supporting Information). The μ_e of the PBDTTPD-HT:ITIC:$PC_{70}BM$ ternary film (2.81×10^{-4} cm^2 V^{-1} s^{-1}) was significantly higher than that of the PBDTTPD-HT:ITIC film (1.98×10^{-4} cm^2 V^{-1} s^{-1}), indicating the positive effect of $PC_{70}BM$ on electron mobility. Intriguingly, the incorporation of $PC_{70}BM$ also yielded improved μ_h of the ternary films (Table S6, Supporting Information). The fraction

Table 1. Summary of photovoltaic properties.

Active layer	Types	V_{OC} [V]	J_{SC} [mA cm^{-2}]	$J_{calc.}$[c)] [mA cm^{-2}]	FF	PCE [%] (PCE$_{ave}$)[d)]
PBDTTPD-HT:ITIC[a)]	Binary	0.97 (0.97 ± 0.01)	14.86 (14.70 ± 0.39)	14.99	0.69 (0.69 ± 0.01)	9.95 (9.75 ± 0.17)
PBDTTPD-HT:PC$_{70}$BM[a)]	Binary	0.86 (0.86 ± 0.01)	12.09 (11.90 ± 0.14)	11.95	0.75 (0.75 ± 0.01)	7.78 (7.65 ± 0.14)
PBDTTPD-HT:PC$_{60}$BM[a)]	Binary	0.88 (0.88 ± 0.01)	10.23 (10.22 ± 0.12)	10.13	0.77 (0.75 ± 0.02)	7.01 (6.77 ± 0.24)
PBDTTPD-HT:ITIC:PC$_{70}$BM[b)]	Ternary	0.95 (0.95 ± 0.01)	17.38 (17.13 ± 0.33)	17.80	0.74 (0.74 ± 0.01)	12.09 (11.86 ± 0.16)
PBDTTPD-HT:ITIC:PC$_{60}$BM[b)]	Ternary	0.96 (0.95 ± 0.01)	17.17 (16.72 ± 0.39)	17.17	0.73 (0.73 ± 0.01)	11.96 (11.67 ± 0.25)

[a)]1:1.5 w/w; [b)]1:0.9:0.6 w/w; [c)]J_{SC} calculated from EQE; [d)]The average and standard deviation values in parentheses are obtained from ten devices.

of PBDTTPD-HT was identical in all the ternary and binary active layers studied and, hence, we posited that this improvement resulted from the influence of PC$_{70}$BM on the morphology of the ternary films.

The charge generation and extraction properties of the ternary and binary devices were further investigated by considering their photocurrent density–effective voltage (J_{ph}–V_{eff}) characteristics. Here, J_{ph} is estimated from J_L–J_D, where J_L and J_D represent the current density under light and in the dark, respectively. V_{eff} is determined from V_0–V, where V_0 is the voltage at which $J_L = J_D$ and V is the bias.[26,27] As shown in Figure 2e, the J_{ph} values of each device were saturated at a V_{eff} of 3 V. The assumption is that, under a sufficiently high effective-voltage regime ($V_{eff} > 3$ V), the dissociated photogenerated excitons (electron–hole pairs) all contribute to the current. Therefore, the saturated current density (J_{sat}) is proportional to the maximum charge generation rate (G_{max}).[26,27] G_{max} values of 1.09×10^{28}, 9.06×10^{27}, and 7.25×10^{27} m^{-3} s^{-1} were calculated for the PBDTTPD-HT:ITIC:PC$_{70}$BM ternary device, the PBDTTPD-HT:ITIC binary device, and the PBDTTPD-HT:PC$_{70}$BM binary device, respectively. The considerably higher G_{max} value of the ternary device corresponds to a more favorable morphology for charge generation (i.e., higher interfacial area for exciton dissociation) compared with that of the binary devices. Charge transport in the devices was investigated by determining the charge extraction probability under the short-circuit condition ($P_C = J_{ph}/J_{sat}$). P_C values of 98%, 93%, and 99% were determined for the ternary device, the PBDTTPD-HT:ITIC binary device, and the PBDTTPD-HT:PC$_{70}$BM binary device, respectively (the FF values of the respective devices are shown in Table 1). The charge generation and extraction associated with the PBDTTPD-HT:ITIC:PC$_{70}$BM ternary device were both superior to those of the PBDTTPD-HT:ITIC device. The same trend was observed for the PBDTTPD-HT:ITIC:PC$_{60}$BM ternary devices (Figure S8, Supporting Information). The enhanced electron transport, owing to the incorporation of PC$_{70}$BM (or PC$_{60}$BM), is attributable to their high electron mobilities. However, the significant improvement in the charge generation and hole mobility resulted from the morphological improvement of the ternary blends, owing to fullerene incorporation.

The J_{SC} and V_{OC} with respect to light intensity were investigate to elucidate the nongeminate recombination in the devices (Figure S9, Supporting Information). As the slope value (α) in J_{SC} versus light intensity plots close to 1, the degree of bimolecular recombination becomes less. All devices showed the α value of 1 indicating negligible bimolecular recombination at the short-circuit condition (Figure S9, Supporting Information). As the slope value (k_BT/q) in V_{OC} versus light intensity plots close to 1 k_BT/q, the smaller trap-assisted recombination occurs in the devices. The PBDTTPD-HT:PC$_{70}$BM device exhibited a slope of 1.41 k_BT/q, while the PBDTTPD-HT:ITIC and PBDTTPD-HT:ITIC:PC$_{70}$BM devices showed the slope of ≈1.0 k_BT/q. This result indicates that the addition of fullerene does not increase the trap-assisted recombination in the devices.

2.3. Working Mechanism of Ternary Devices

The exciton dissociation efficiency was further evaluated via photoluminescence (PL) emission spectra of the PBDTTPD-HT:ITIC:PC$_{70}$BM ternary active layers (**Figure 3**). When the films were excited at 560 nm (Figure 3a), where major absorption by PBDTTPD-HT occurs, the emission at 670 nm was quenched completely in each film. This indicated that the excitons generated by PBDTTPD-HT were almost quantitatively dissociated in the ternary films. However, the PL emission peaks from ITIC at 760 nm were retained and the intensity varied with the composition of the ternary films. These trends were elucidated by measuring the PL emissions of the films at an excitation wavelength of 710 nm, where absorption only by the ITIC occurs (Figure 3b). The resulting PL emission peaks at 760 nm also varied with the composition of the ternary films. Notably, regardless of the excitation wavelength (560 or 710) nm, the intensity of the emission peaks decreased almost linearly with increasing fraction of PC$_{70}$BM in the films, although the basis for this decrease remained unclear. In other words, this decrease could be attributed to additional charge transfer from ITIC to PC$_{70}$BM or the lower fraction of ITIC in the PBDTTPD-HT:ITIC:PC$_{70}$BM ternary films compared with that in the PBDTTPD-HT:ITIC binary film.

The occurrence of charge transfer between the ITIC and PC$_{70}$BM in the ternary systems was further investigated by obtaining PL emission spectra of the ITIC:PC$_{70}$BM acceptor blend films with various ratios (Figure 3d). The ITIC:PC$_{70}$BM blend films were excited at 710 nm where ITIC absorption occurs, and the emission at 760 nm was monitored. Excitation at 710 nm was characterized by strong PL emission and no emission from the pristine ITIC film and the pristine PC$_{70}$BM film, respectively. The emission decreased almost linearly with increasing fraction of PC$_{70}$BM. This result

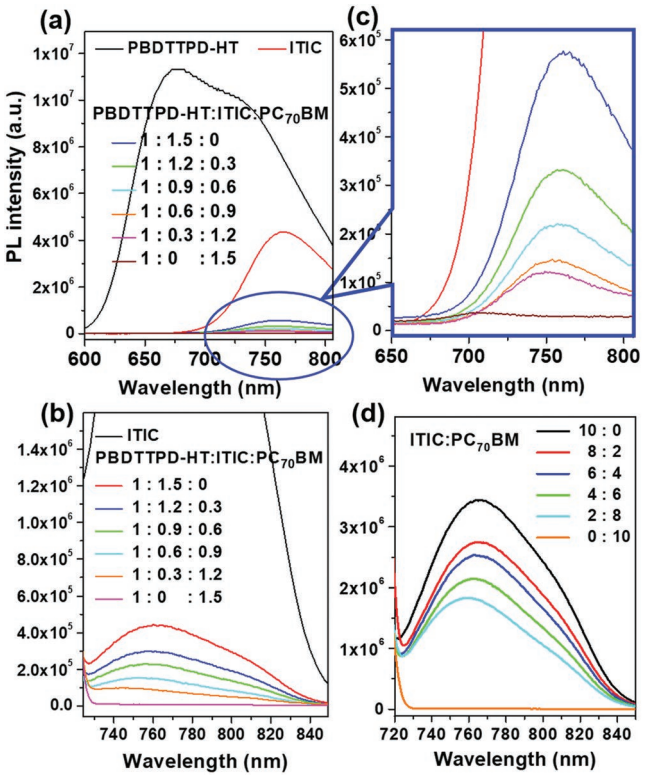

Figure 3. PL emission spectra of various PBDTTPD-HT:ITIC:$PC_{70}BM$ ternary films excited at a) 560 nm or b) 710 nm; c) amplified spectra of (a); and d) PL emission spectra of various ITIC:$PC_{70}BM$ binary films excited at 710 nm.

revealed that the ITIC and $PC_{70}BM$ are photophysically independent, without the occurrence of internal charge or energy transfer,[5,24] and the operation of our ternary devices is described by a parallel-like model.[20,24,28] The PL emission measurement of PBDTTPD-HT:ITIC:$PC_{60}BM$ ternary films and ITIC:$PC_{60}BM$ blend films yielded the same trend, thereby confirming the working mechanism of these ternary devices (Figure S7, Supporting Information). The parallel-like ternary indicated that the charges are generated independently at either PBDTTPD-HT:ITIC or PBDTTPD-HT:fullerene interfaces, and collected through respective domains (Figure 6). Therefore, the enhanced EQE of ternary devices at the NIR regime is attributed to morphology modification induced by fullerene incorporation.

2.4. Morphological Effects of Fullerenes on Ternary Devices

The charge generation in the ternary devices (i.e., higher G_{max}) was higher than that of the PBDTTPD-HT:ITIC binary device despite the lower optical absorption (Figure 2d,e; Figure S5, Supporting Information). This implied that the inclusion of fullerenes increases the donor/acceptor interfacial area through modification of the morphology. The morphology of the binary and the ternary BHJ layers was investigated via transmission electron microscopy (TEM) and atomic force microscopy (AFM). A TEM image of the PBDTTPD-HT:$PC_{70}BM$ binary film (**Figure 4**f) revealed large dark aggregates, a typical feature of the $PC_{70}BM$-rich region. However, due to the high miscibility between PBDTTPD-HT and ITIC, discernable segregation was absent from the PBDTTPD-HT:ITIC binary film. The $PC_{70}BM$ aggregates in the PBDTTPD-HT:ITIC:$PC_{70}BM$ ternary film were uniformly distributed and considerably finer than those in the binary film (Figure 4e). The AFM images of the binary and the ternary BHJ films are consistent with the TEM results (Figure 4a–c). Compared with the PBDTTPD-HT:ITIC film, which exhibited no discernible domain segregation, the PBDTTPD-HT:$PC_{70}BM$ film was characterized by the segregation of soft (PBDTTPD-HT) and hard ($PC_{70}BM$) domains and exhibited higher surface roughness (Figure 4a,c). The root-mean-square roughness (R_{RMS}) of the PBDTTPD-HT:ITIC and PBDTTPD-HT:$PC_{70}BM$ binary films was 0.171 and 1.75 nm, respectively. In the ternary films, the segregation of soft and hard domains is finer, owing possibly to the smaller $PC_{70}BM$ aggregates (Figure 4b) compared with those occurring in the binary films. These finer $PC_{70}BM$ aggregates in the ternary films might facilitate exciton dissociation due to the enhanced interfacial area. Moreover, the charge mobility study results (Figures S10 and S11, Supporting Information) indicate that the fine $PC_{70}BM$ domains are sufficiently continuous to facilitate charge transport in parallel-like ternary layers.

The characteristics of molecular ordering in the ternary active layers were investigated via 2D grazing incidence, wide angle X-ray diffraction (GIWAXS).[29,30] **Figure 5**a–e shows the 2D GIWAXS patterns of pristine PBDTTPD-HT, pristine ITIC,

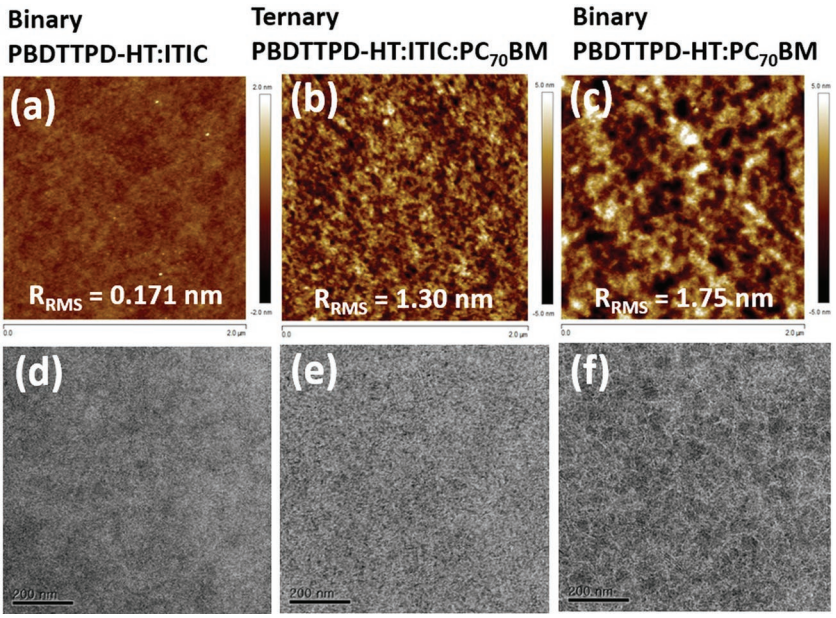

Figure 4. Atomic force microscopy and transmission electron microscopy of a,d) PBDTTPD-HT:ITIC (1:1.5 w/w) binary films, b,e) PBDTTPD-HT:ITIC:$PC_{70}BM$ (1:0.9:0.6 w/w) ternary films, and c,f) PBDTTPD-HT:$PC_{70}BM$ (1:1.5 w/w) binary films.

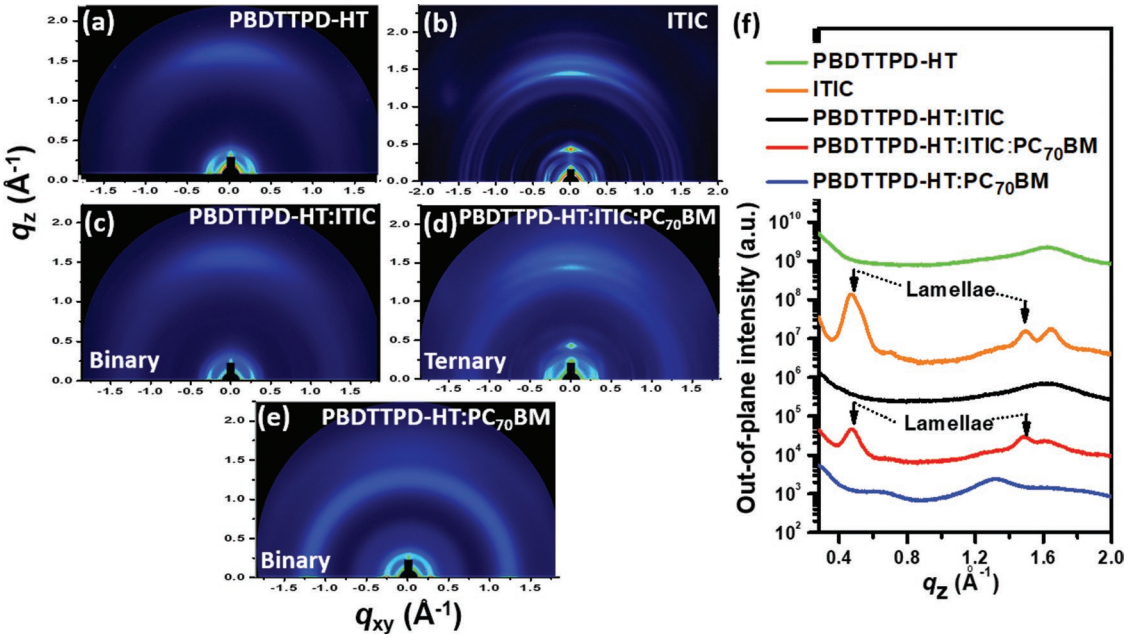

Figure 5. 2D GIWAXS patterns of pristine a) PBDTTPD-HT, b) ITIC films, c) PBDTTPD-HT:ITIC (1:1.5 w/w) binary films, d) PBDTTPD-HT:ITIC:$PC_{70}BM$ (1:0.9:0.6 w/w) ternary films, and e) PBDTTPD-HT:$PC_{70}BM$ (1:1.5 w/w) binary films. f) Out-of-plane line cut of corresponding 2D GIWAXS patterns.

and the corresponding binary/ternary blend films, respectively. The line-cut intensities taken along the *out-of-plane* direction in the 2D GIWAXS patterns are shown in Figure 5f. The pristine PBDTTPD-HT exhibited *out-of-plane* (010) diffraction, indicating that the π–π stacking is oriented in a face-on mode along the Qz axis at 1.622 $Å^{-1}$, corresponding to a *d*-spacing of 3.87 Å (Figure 5a). The pristine ITIC film shows strong symmetric ordering of its lamellae. This interpretation was based on the peak position ratio of 1:3 relative to the primary *out-of-plane* peak at $q_z \cong 0.470$ and 1.486 $Å^{-1}$ (Figure 5b,f), as well as the π–π stacking in the face-on mode along the q_z axis at $q_z \cong 1.644$ $Å^{-1}$, corresponding to a *d*-spacing of 3.82 Å. Although weak π–π stacking diffraction was discernible, the characteristic ITIC lamellae ordering is absent from the PBDTTPD-HT:ITIC binary film, indicating good miscibility between PBDTTPD-HT and ITIC (Figure 5c).[25] The 2D GIWAXD pattern of the PBDTTPD-HT:$PC_{70}BM$ binary film consisted, however, of only an azimuthally isotropic ring pattern resulting from $PC_{70}BM$ aggregation, with no apparent face-on stacking peaks (Figure 5e). Notably, in the case of the PBDTTPD-HT:ITIC:$PC_{70}BM$ ternary films, the characteristic molecular orientation peaks from ITIC (lamellae ordering and π–π stacking) reappeared (Figure 5d). These results revealed that the incorporation of $PC_{70}BM$ into the PBDTTPD-HT:ITIC binary blend may have mediated reassembly of ITIC in the ternary films. Furthermore, ITIC reassembly occurred in the PBDTTPD-HT:ITIC:$PC_{70}BM$ ternary films within a range of ITIC:$PC_{70}BM$ ratios (Figure S12, Supporting Information). We attributed the reordering of ITIC by addition of $PC_{70}BM$ to the lower miscibility between ITIC and $PC_{70}BM$ compared to that between PBDTTPD-HT and ITIC. The identical trend, i.e., molecular ordering in the $PC_{60}BM$-based ternary films, confirmed the general effect of fullerenes on the morphology of our ternary systems (Figures S13 and S14, Supporting Information). The incorporation of fullerenes resulted in modification of the morphology and enhanced ITIC ordering, while the domains of ITIC and $PC_{70}BM$ were still sufficiently continuous to transport electrons. A schematic showing the morphological evolution (finer segregation than in the binary systems and reassembly of ITIC) in the ternary films is shown in **Figure 6**.

The optimized morphology of the ternary devices showed sufficient storage stability. As shown in Figure S15 (Supporting Information), the storage stability of unencapsulated PBDTTPD-HT:ITIC:$PC_{70}BM$ ternary device under nitrogen environment was higher than that of binary devices (PBDTTPD-HT:ITIC and PBDTTPD-HT:$PC_{70}BM$) after 580 h. This result indicated that the well-dispersed morphology of ternary blends was kept stable compared to the binary blends.

2.5. Energy Loss in Ternary Devices

Previous studies have reported that the V_{OC} of ternary devices is determined by the composition of the active materials.[20,24,28,31–33] In a recent study,[34–36] the V_{OC} of ternary devices was determined from the effective energy levels of the binary acceptors, which vary with the energy levels and the ratio of the individual acceptors (fullerene and nonfullerene).[34] However, in the case of energy transfer among components, the V_{OC} is determined by the lower of the two values associated with the individual binary devices.[19,37] Although considerable fractions of fullerenes were incorporated, the V_{OC} values of our ternary devices (0.95 and 0.96 V) were slightly lower than that of the PBDTTPD-HT:ITIC binary device (0.97 V), a trend which differs from that previously reported for ternary devices.[38,39] The E_{loss} values of PBDTTPD-HT:ITIC:$PC_{70}BM$

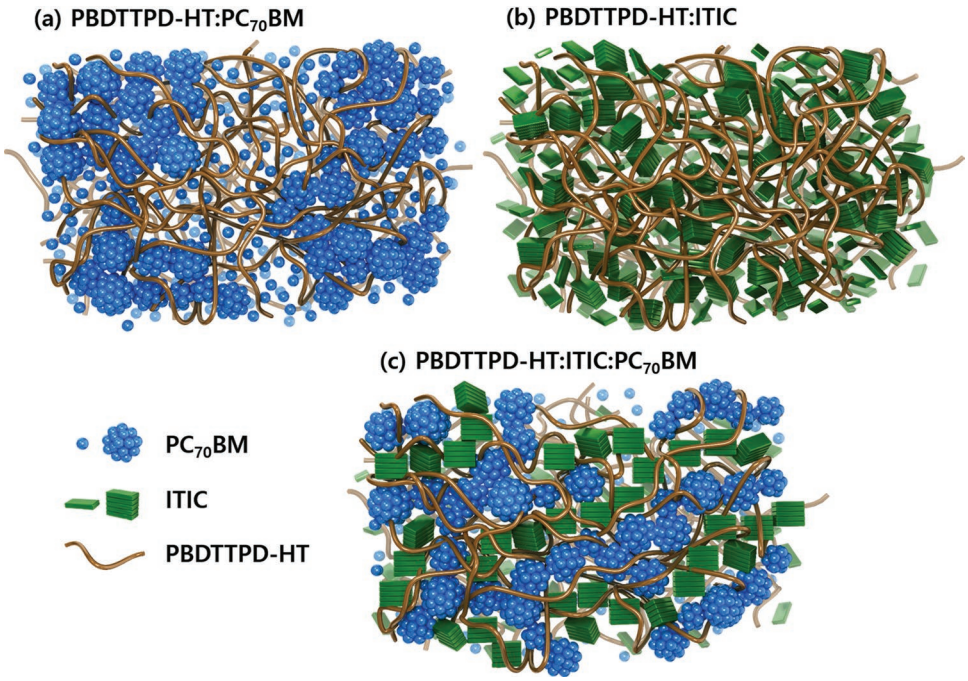

Figure 6. Schematic showing the morphology change and reassembly of ITIC in PBDTTPD-HT:ITIC:$PC_{70}BM$ ternary films. a) PBDTTPD-HT:$PC_{70}BM$ and b) PBDTTPD-HT:ITIC blend films with weak ordering, and c) the combination of two acceptors ($PC_{70}BM$ and ITIC) leads to modification of the morphology, enhancement of the ordering, and formation of a bicontinuous network morphology.

and PBDTTPD-HT:ITIC:$PC_{60}BM$ were only 0.61 and 0.60 eV, respectively. We attributed this remarkably low additional energy loss of the ternary devices to changes in the effective donor:acceptor ratio. Generally, the V_{OC} of OPV devices is influenced by their donor:acceptor ratio, which alters the charge transfer state of the active layers.[40] This hypothesis was verified by fabricating binary devices with various donor:acceptor ratios, and determining the V_{OC} dependence on this ratio (Figures S2–S4 and S16 and Tables S1–S3, Supporting Information). The V_{OC} of the PBDTTPD-HT:$PC_{70}BM$ and PBDTTPD-HT:ITIC devices varied from 0.86 to 0.95 V and 0.97 to 1.0 V, respectively, when the donor:acceptor ratios were varied from 1:1.5 to 1:0.3 w/w (Figures S2 and S4, Supporting Information). For example, the V_{OC} values of the PBDTTPD-HT:ITIC (1:0.9 w/w) device and PBDTTPD-HT:$PC_{70}BM$ (1:0.6 w/w) device were 1.0 and 0.93 V, respectively. Based on the results, the low V_{OC} deficit of the ternary device was attributed to changes in the effective donor:acceptor ratio of the active layers.

3. Conclusion

The morphology optimization of the PBDTTPD-HT:ITIC binary active layer via the incorporation of fullerenes yielded substantial improvement in the performance of ternary OPV devices. The ternary blends including ITIC and fullerene were parallel-linked without charge or energy transfer. In addition, the incorporated fullerenes were uniformly dispersed as fine aggregates mediating the ordering of ITIC and were sufficiently continuous for the efficient transport of electrons. This morphological modification resulted in simultaneous enhancement of the charge generation and extraction in the ternary devices. Furthermore, the PCE values realized for the PBDTTPD-HT:ITIC:$PC_{70}BM$ and PBDTTPD-HT:ITIC:$PC_{60}BM$ devices (12.09% and 11.96%, respectively) were higher than that of the PBDTTPD-HT:ITIC binary device (9.95%). Moreover, owing to careful changes in the donor:acceptor composition of the ternary blends, the additional energy loss of the ternary devices was only marginal compared with that of the PBDTTPD-HT:ITIC binary device.

4. Experimental Section

Materials and Methods: Each ITO substrate was cleaned for 10 min via ultrasonication in acetone and isopropyl alcohol (IPA). Bulk heterojunction devices were fabricated using an inverted structure (ITO/ZnO/BHJ/MoO_x/Ag). In the first step of the process, ZnO was prepared as the electron transporting layer (≈20 nm) via in situ ZnO sol–gel conversion, in accordance with a reported procedure. For the precursor, a 0.45 M solution of zinc acetate dehydrate ($[Zn(CH_3COO)_2{\cdot}2H_2O]$, Sigma Aldrich, 99.9%, 5 g) and ethanolamine ($NH_2CH_2CH_2OH$, Sigma Aldrich, 99.5%, 1.35 mL) in 2-methoxyethanol ($CH_3OCH_2CH_2OH$, Sigma Aldrich, 99.8%, 50 mL) were spin-coated at 4000 rpm for 15 s under ambient conditions, and then thermally annealed from room temperature to 200 °C for 10 min. The active layers were fabricated under N_2 in a glove box. The BHJ active layers were prepared through the spin-coating of various active solutions. The concentration of each active solution in chloroform was 7.5 mg mL^{-1}, and 0.8 vol% of 1,8-diiodooctane (DIO, TCI) was used as an additive. Afterward, the solutions were stirred for 2 h under N_2 prior to coating. In addition, the polymer donor (PBDTTPD-HT) and a small molecule NFA (ITIC) were synthesized in

accordance with previous reports.[1–3] The $PC_{70}BM$ and $PC_{60}BM$ were purchased from the EM Index. Thin electron blocking layers of MoO_x (8 nm) and a metal electrode (Ag, 150 nm) were deposited via thermal evaporation under low pressure (10^{-6} bar).

Device Analysis: The *J–V* characteristics of the BHJ devices were measured using a Keithley 2401 instrument and a solar simulator with a 150 W xenon lamp (Newport) as the light source. The light intensity was set to AM 1.5 G and calibrated using a KG5 monosilicon standard from the National Renewable Energy laboratory (NREL). The EQE spectra were obtained by passing a 400 W xenon lamplight through a monochromator using a filter of appropriate wavelength (Mc Science, K3100 IQX). The chopping frequency (i.e., 5 Hz) was measured from 300 to 950 nm. Photoluminescence measurements were performed using an SPEX Nanolog 3-211 (Horriba). The signal was analyzed using a NIR spectrometer equipped with an FL-1073 (R928 UV–vis PMT detector). The space charge–limited current was used to measure the charge mobility of the active layers. Measurements were performed in the dark. A hole-only device (ITO/PEDOT:PSS/active layer/MoO_x/Ag) and an electron-only device (ITO/ZnO/active layer/ZnO/Al) were used to measure the hole and electron mobility. The mobility was calculated, via the Mott–Gurney law, in an SCLC trap-free regime. The layer thickness of OPV devices was determined by scanning electron microscopy (SEM). The thickness of the active layer was ≈100 nm (Figure S17, Supporting Information).

Sample Analysis: Cyclic voltammetry was performed on a BAS 100B/W electrochemical analyzer with a three-electrode cell in a 0.1 N Bu_4NBF_4 solution in acetonitrile (scan rate: 50 mV s^{-1}). The PBDTTPD-HT, ITIC, and $PC_{70}BM$ were coated onto a Pt wire electrode by dipping the electrode into each solution in chloroform. All measurements were calibrated against an internal standard of ferrocene (Fc), the ionization potential (IP) value (i.e., −4.8 eV for the Fc/Fc^+ redox system). AFM scan images (2 µm × 2 µm) were acquired in tapping mode on a Nanoscope instrument (Bruker), and TEM images were obtained on a JEM-2100F (JEOL LTD.).

The 2D Grazing Incidence Wide-Angle X-Ray Diffraction (2D-GIWAXS): 2D-GIWAXS measurements were performed at Beamline 9A of the Pohang Accelerator Laboratory (PAL), Korea. A beam energy, sample-to-detector distance, and incidence angle (α_i, for full-depth information about the samples) of 11.055 keV, 221 mm, and 0.12°, respectively, were employed.

Supporting Information

Supporting Information is available from the Wiley Online Library or from the author.

Acknowledgements

W.T.H. and F.T.A.W. contributed equally to this work. The authors gratefully acknowledge support from the New and Renewable Energy Core Technology Program of the Korea Institute of Energy Technology Evaluation and Planning (KETEP), granted financial resources from the Ministry of Trade, Industry and Energy, Republic of Korea (Grant No. 20163030013960), the National Research Foundation (NRF) Grant funded by the Korean Government (MSIP, Grant Nos. 2016R1A5A1012966 and 2017R1A2B2009178), and the Global Scholarship Program for Foreign Graduate Students at Kookmin University in Korea.

Conflict of Interest

The authors declare no conflict of interest.

Keywords

low energy loss, nanomorphology, nonfullerene acceptor, organic photovoltaic device, parallel-linked ternary

Received: December 9, 2018
Revised: January 6, 2019
Published online:

[1] Y. Lin, J. Wang, Z.-G. Zhang, H. Bai, Y. Li, D. Zhu, X. Zhan, *Adv. Mater.* **2015**, *27*, 1170.
[2] Y. Qin, M. A. Uddin, Y. Chen, B. Jang, K. Zhao, Z. Zheng, R. Yu, T. J. Shin, H. Y. Woo, J. Hou, *Adv. Mater.* **2016**, *28*, 9416.
[3] W. Zhao, D. Qian, S. Zhang, S. Li, O. Inganäs, F. Gao, J. Hou, *Adv. Mater.* **2016**, *28*, 4734.
[4] Y. Lin, F. Zhao, Q. He, L. Huo, Y. Wu, T. C. Parker, W. Ma, Y. Sun, C. Wang, D. Zhu, A. J. Heeger, S. R. Marder, X. Zhan, *J. Am. Chem. Soc.* **2016**, *138*, 4955.
[5] Y. Yang, Z.-G. Zhang, H. Bin, S. Chen, L. Gao, L. Xue, C. Yang, Y. Li, *J. Am. Chem. Soc.* **2016**, *138*, 15011.
[6] Y. Cui, H. Yao, B. Gao, Y. Qin, S. Zhang, B. Yang, C. He, B. Xu, J. Hou, *J. Am. Chem. Soc.* **2017**, *139*, 7302.
[7] S. Li, L. Ye, W. Zhao, S. Zhang, S. Mukherjee, H. Ade, J. Hou, *Adv. Mater.* **2016**, *28*, 9423.
[8] T. Ameri, P. Khoram, J. Min, C. J. Brabec, *Adv. Mater.* **2013**, *25*, 4245.
[9] Z. Y. Wang, Y. J. Zhang, J. Q. Zhang, Z. X. Wei, W. Ma, *Adv. Energy Mater.* **2016**, *6*, 1502456.
[10] W. Zhao, S. Li, S. Zhang, X. Liu, J. Hou, *Adv. Mater.* **2017**, *29*, 1604059.
[11] Z. Zhou, S. Xu, J. Song, Y. Jin, Q. Yue, Y. Qian, F. Liu, F. Zhang, X. Zhu, *Nat. Energy* **2018**, *3*, 952.
[12] G. Ding, J. Yuan, F. Jin, Y. Zhang, L. Han, X. Ling, H. Zhao, W. Ma, *Nano Energy* **2017**, *36*, 356.
[13] L. Nian, Y. Kan, H. Wang, K. Gao, B. Xu, Q. Rong, R. Wang, J. Wang, F. Liu, J. Chen, G. Zhou, T. P. Russell, A. K. Y. Jen, *Energy Environ. Sci.* **2018**, *11*, 3392.
[14] L. Lu, T. Xu, W. Chen, E. S. Landry, L. Yu, *Nat. Photonics* **2014**, *8*, 716.
[15] L. Lu, W. Chen, T. Xu, L. Yu, *Nat. Commun.* **2015**, *6*, 7327.
[16] Y. Yang, W. Chen, L. Dou, W.-H. Chang, H.-S. Duan, B. Bob, G. Li, Y. Yang, *Nat. Photonics* **2015**, *9*, 190.
[17] J. Zhang, Y. Zhang, J. Fang, K. Lu, Z. Wang, W. Ma, Z. Wei, *J. Am. Chem. Soc.* **2015**, *137*, 8176.
[18] N. Gasparini, X. Jiao, T. Heumueller, D. Baran, G. J. Matt, S. Fladischer, E. Spiecker, H. Ade, C. J. Brabec, T. Ameri, *Nat. Energy* **2016**, *1*, 16118.
[19] T. Liu, L. Huo, X. Sun, B. Fan, Y. Cai, T. Kim, J. Y. Kim, H. Choi, Y. Sun, *Adv. Energy Mater.* **2016**, *6*, 1502109.
[20] Y. Yang, W. Chen, L. T. Dou, W. H. Chang, H. S. Duan, B. Bob, G. Li, Y. Yang, *Nat. Photonics* **2015**, *9*, 190.
[21] J. Mai, T.-K. Lau, J. Li, S.-H. Peng, C.-S. Hsu, U. S. Jeng, J. Zeng, N. Zhao, X. Xiao, X. Lu, *Chem. Mater.* **2016**, *28*, 6186.
[22] N. Gasparini, M. Salvador, S. Fladischer, A. Katsouras, A. Avgeropoulos, E. Spiecker, C. L. Chochos, C. J. Brabec, T. Ameri, *Adv. Energy Mater.* **2015**, *5*, 1501527.
[23] H. Lu, J. C. Zhang, J. Y. Chen, Q. Liu, X. Gong, S. Y. Feng, X. J. Xu, W. Ma, Z. S. Bo, *Adv. Mater.* **2016**, *28*, 9559.
[24] T. Liu, X. Xue, L. Huo, X. Sun, Q. An, F. Zhang, T. P. Russell, F. Liu, Y. Sun, *Chem. Mater.* **2017**, *29*, 2914.
[25] W. T. Hadmojo, F. T. A. Wibowo, D. Y. Ryu, I. H. Jung, S.-Y. Jang, *ACS Appl. Mater. Interfaces* **2017**, *9*, 32939.

[26] P. W. M. Blom, V. D. Mihailetchi, L. J. A. Koster, D. E. Markov, *Adv. Mater.* **2007**, *19*, 1551.
[27] Z. Li, J. D. A. Lin, H. Phan, A. Sharenko, C. M. Proctor, P. Zalar, Z. Chen, A. Facchetti, T.-Q. Nguyen, *Adv. Funct. Mater.* **2014**, *24*, 6989.
[28] L. Yang, H. Zhou, S. C. Price, W. You, *J. Am. Chem. Soc.* **2012**, *134*, 5432.
[29] T. Goh, J.-S. Huang, K. G. Yager, M. Y. Sfeir, C.-Y. Nam, X. Tong, L. M. Guard, P. R. Melvin, F. Antonio, B. G. Bartolome, M. L. Lee, N. Hazari, A. D. Taylor, *Adv. Energy Mater.* **2016**, *6*, 1600660.
[30] J. Rivnay, S. C. B. Mannsfeld, C. E. Miller, A. Salleo, M. F. Toney, *Chem. Rev.* **2012**, *112*, 5488.
[31] P. P. Khlyabich, B. Burkhart, B. C. Thompson, *J. Am. Chem. Soc.* **2011**, *133*, 14534.
[32] R. A. Street, D. Davies, P. P. Khlyabich, B. Burkhart, B. C. Thompson, *J. Am. Chem. Soc.* **2013**, *135*, 986.
[33] P. P. Khlyabich, A. E. Rudenko, B. C. Thompson, Y.-L. Loo, *Adv. Funct. Mater.* **2015**, *25*, 5557.
[34] Y. Chen, P. Ye, Z. G. Zhu, X. Wang, L. Yang, X. Xu, X. Wu, T. Dong, H. Zhang, J. Hou, F. Liu, H. Huang, *Adv. Mater.* **2017**, *29*, 1603154.
[35] N. Felekidis, E. Wang, M. Kemerink, *Energy Environ. Sci.* **2016**, *9*, 257.
[36] C. Wang, X. Xu, W. Zhang, S. B. Dkhil, X. Meng, X. Liu, O. Margeat, A. Yartsev, W. Ma, J. Ackermann, E. Wang, M. Fahlman, *Nano Energy* **2017**, *37*, 24.
[37] P. P. Khlyabich, A. E. Rudenko, R. A. Street, B. C. Thompson, *ACS Appl. Mater. Interfaces* **2014**, *6*, 9913.
[38] P. Bi, T. Xiao, X. Yang, M. Niu, Z. Wen, K. Zhang, W. Qin, S. K. So, G. Lu, X. Hao, H. Liu, *Nano Energy* **2018**, *46*, 81.
[39] L. Zhan, S. Li, H. Zhang, F. Gao, T.-K. Lau, X. Lu, D. Sun, P. Wang, M. Shi, C.-Z. Li, H. Chen, *Adv. Sci.* **2018**, *5*, 1800755.
[40] D. Veldman, Ö. İpek, S. C. J. Meskers, J. Sweelssen, M. M. Koetse, S. C. Veenstra, J. M. Kroon, S. S. van Bavel, J. Loos, R. A. J. Janssen, *J. Am. Chem. Soc.* **2008**, *130*, 7721.

ADVANCED FUNCTIONAL MATERIALS

Supporting Information

for *Adv. Funct. Mater.,* DOI: 10.1002/adfm.201808731

Performance Optimization of Parallel-Like Ternary Organic Solar Cells through Simultaneous Improvement in Charge Generation and Transport

Wisnu Tantyo Hadmojo, Febrian Tri Adhi Wibowo, Wooseop Lee, Hye-Kyung Jang, Yeongsik Kim, Septy Sinaga, Minsuk Park, Sang-Yong Ju, Du Yeol Ryu, In Hwan Jung,* and Sung-Yeon Jang**

Supporting Information

Performance Optimization of Parallel-Like Ternary Organic Solar Cells Through Simultaneous Improvement in Charge Generation and Transport

Wisnu Tantyo Hadmojo, Febrian Tri Adhi Wibowo, Wooseop Lee, Hye-Kyung Jang, Yeongsik Kim, Septy Sinaga, Minsuk Park, Sang-Yong Ju, Du Yeol Ryu, In Hwan Jung*, and Sung-Yeon Jang**

((Optional Dedication))

W. T. Hadmojo, F. T. A. Wibowo, S. Sinaga, Prof. I. H. Jung, Prof. S.-Y. Jang
Department of Chemistry, Kookmin University,
77 Jeongneung-ro, Seongbuk-gu, Seoul 136-702, Republic of Korea.
E-mail: ihjung@kookmin.ac.kr and syjang@kookmin.ac.kr

W. Lee, H.-K. Jang, Y. Kim, Prof. D. Y. Ryu
Department of Chemical and Biomolecular Engineering,
Yonsei University, 50 Yonsei-ro, Seodaemun-gu, 03722 Seoul, Republic of Korea.
E-mail: dyryu@yonsei.ac.kr

M. Park, Prof. S.-Y. Ju,
Department of Chemistry, Yonsei University,
50 Yonsei-ro, Seodaemun-gu, Seoul, Republic of Korea

Keywords: organic photovoltaic device, parallel-linked ternary, non-fullerene acceptor, low energy loss, nanomorphology

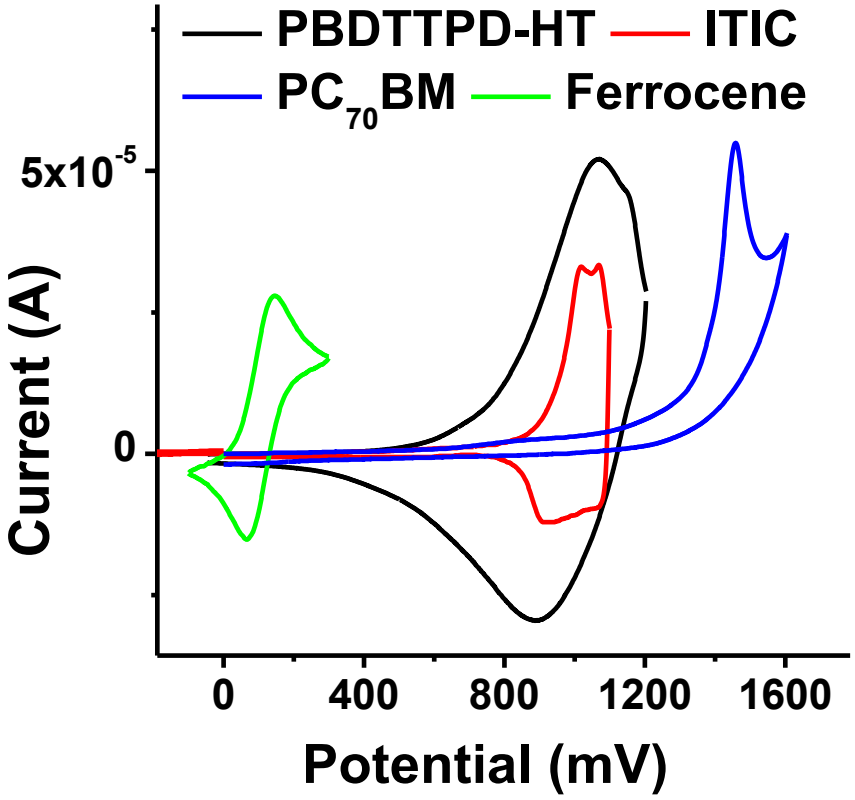

Figure S1. Cyclic voltammograms of PBDTTPD-HT, ITIC, and $PC_{70}BM$.

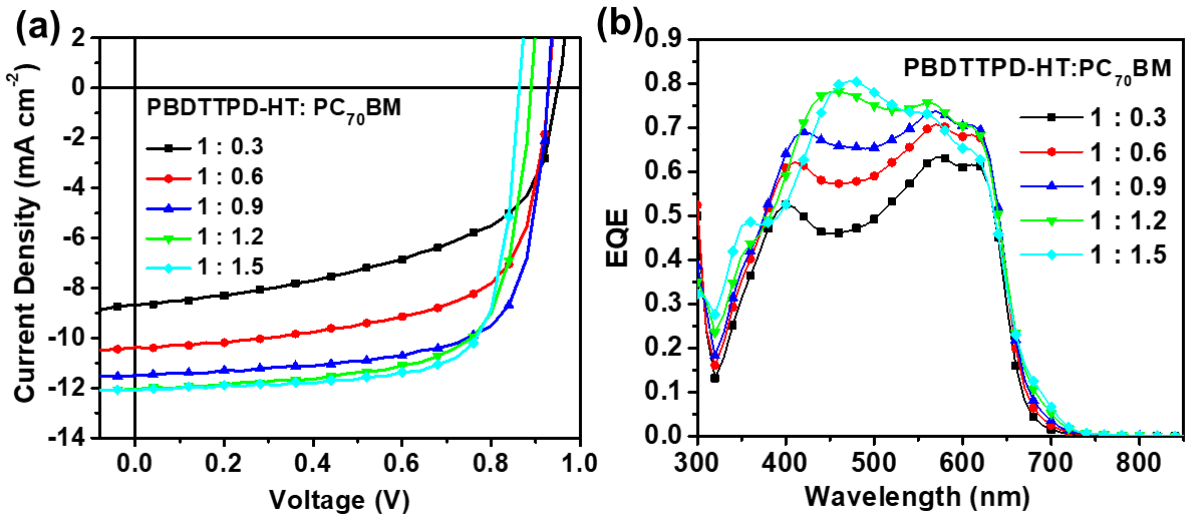

Figure S2. (a) *J-V* characteristics and (b) corresponding EQE spectra of PBDTTPD-HT:$PC_{70}BM$ devices at different weight ratios (w/w).

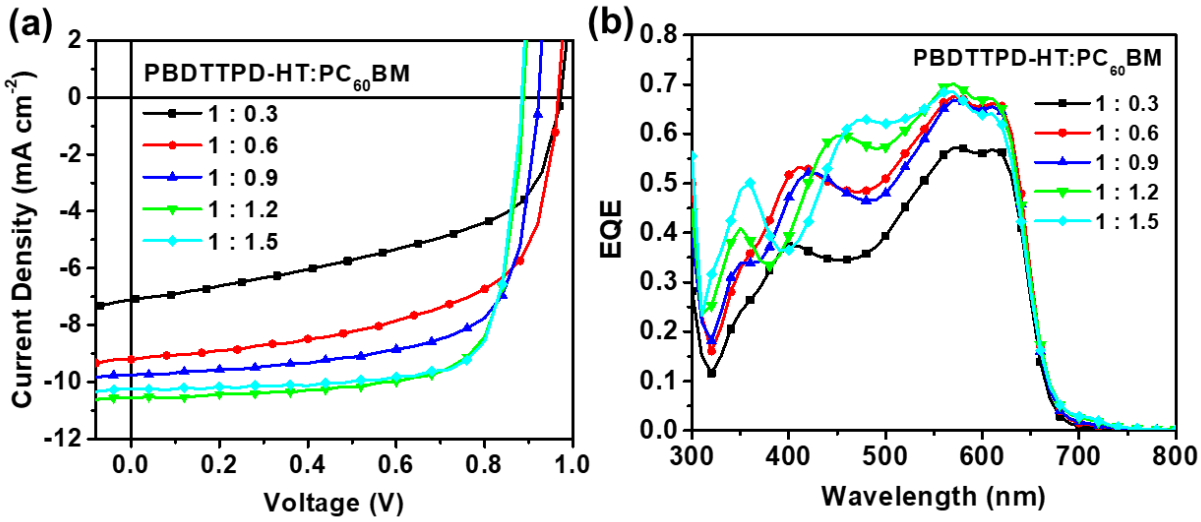

Figure S3. (a) *J-V* characteristics and (b) corresponding EQE spectra of PBDTTPD-HT:$PC_{60}BM$ devices at different weight ratios (w/w).

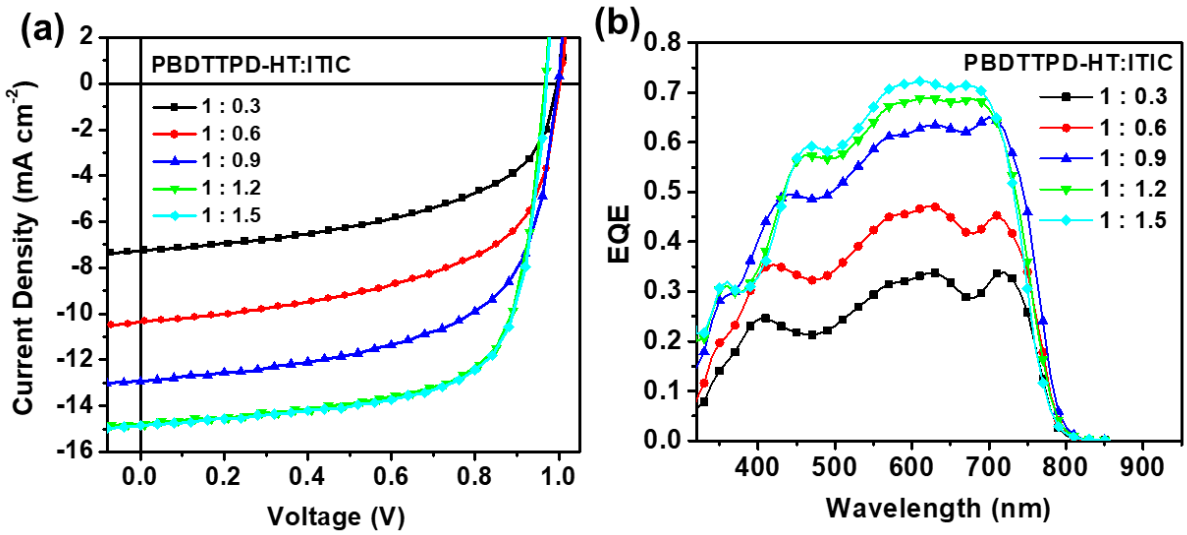

Figure S4. (a) *J-V* characteristics and (b) corresponding EQE spectra of PBDTTPD-HT:ITIC devices at different weight ratios (w/w).

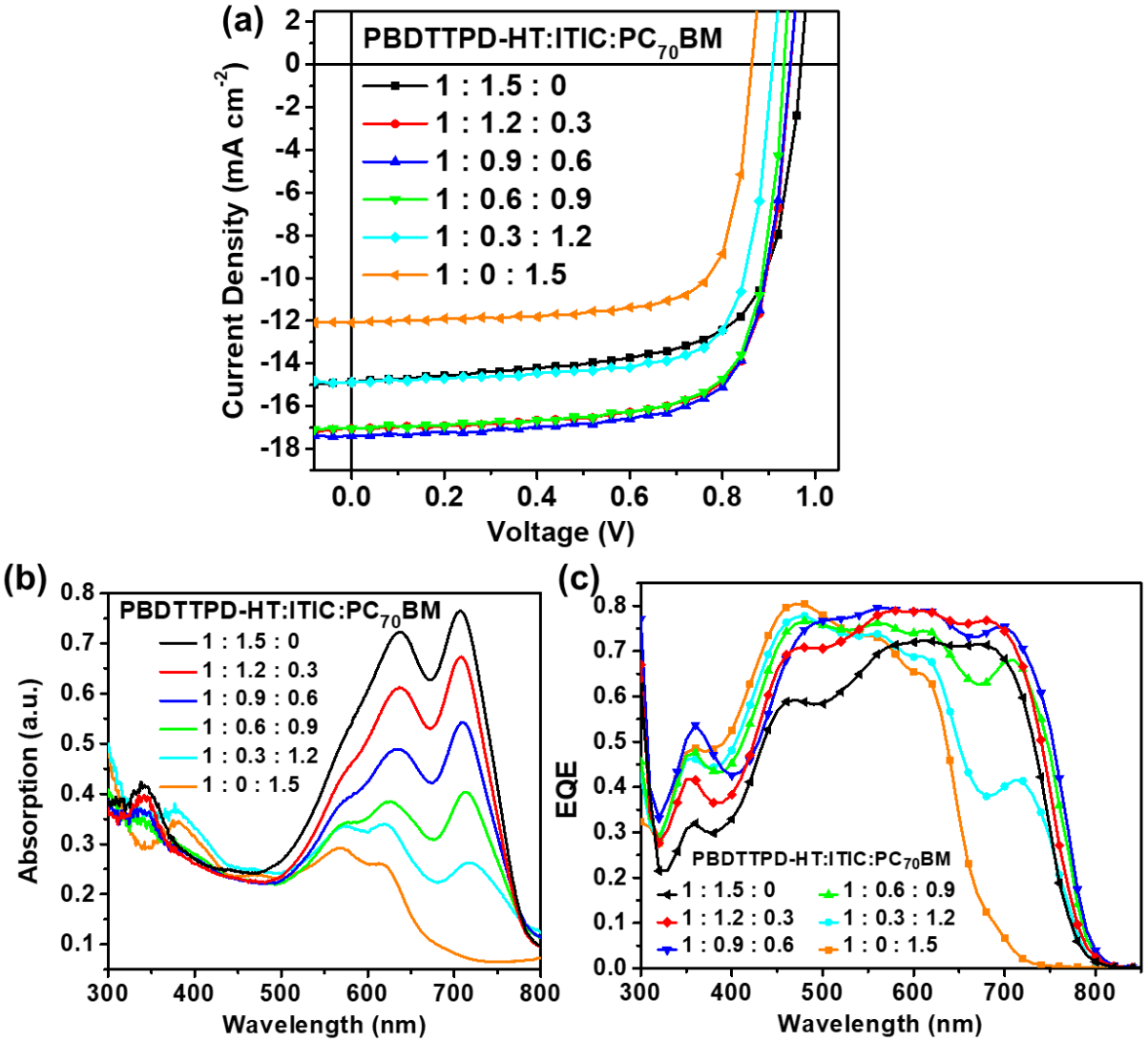

Figure S5. (a), (c) *J-V* characteristics and EQE spectra, respectively, of PBDTTPD-HT:ITIC:$PC_{70}BM$ ternary devices, (b) Ultraviolet visible (UV-vis) absorption spectra of various PBDTTPD-HT:ITIC:$PC_{70}BM$ ternary films.

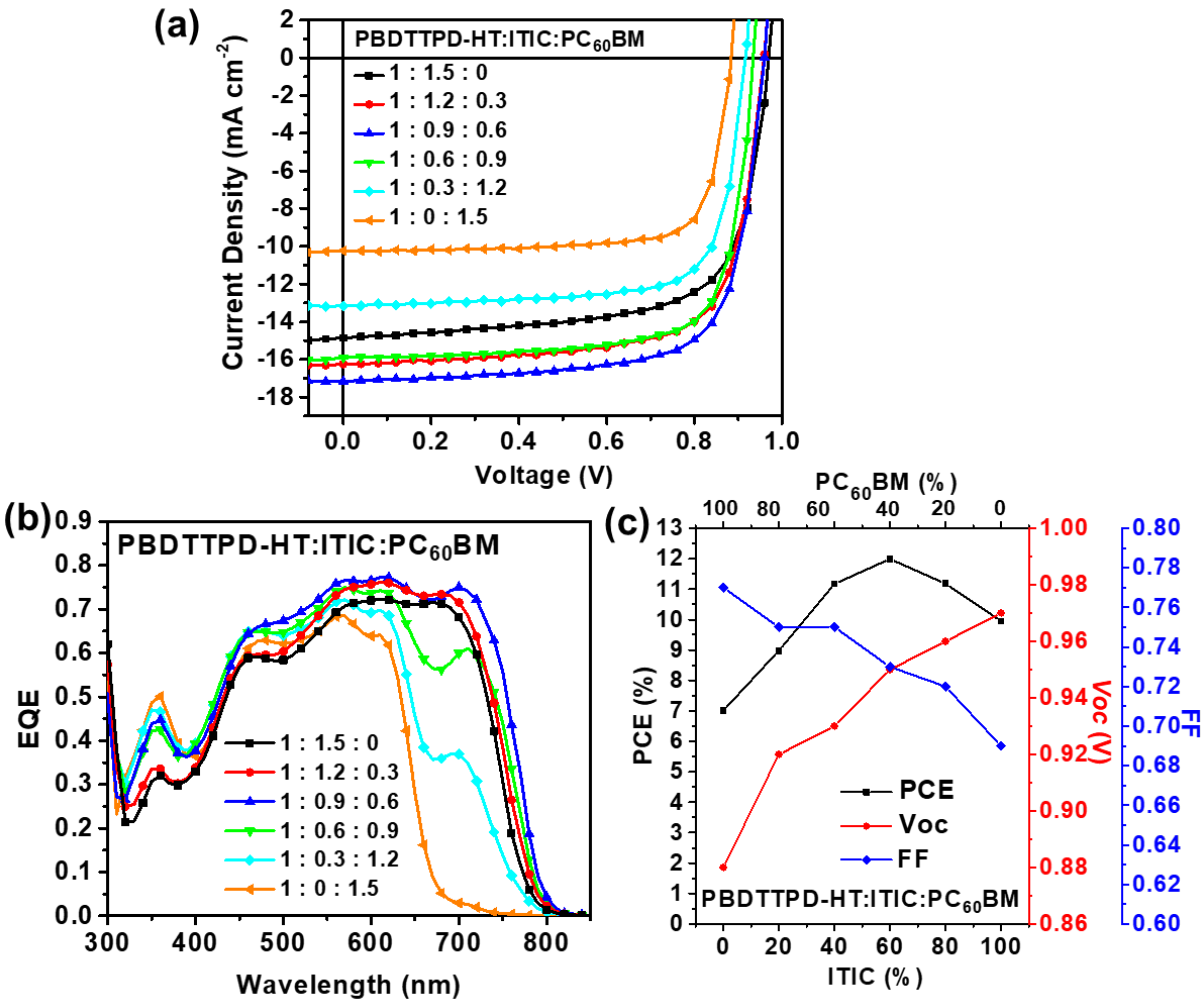

Figure S6. (a) *J-V* characteristics and (b) EQE spectra of PBDTTPD-HT:ITIC:$PC_{60}BM$ ternary devices; (c) Composition dependence of PCE, V_{OC}, and FF associated with the ternary devices.

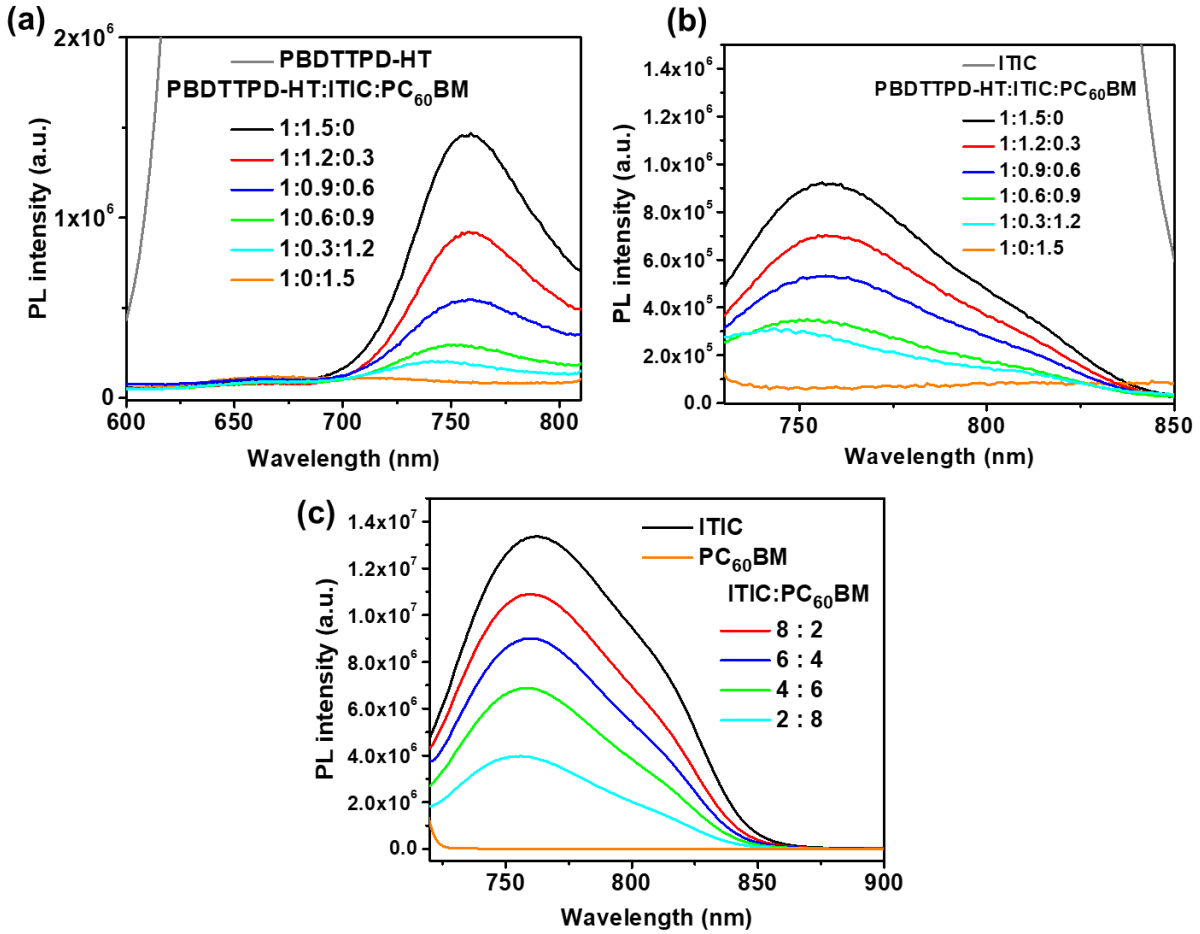

Figure S7. PL emission spectra of various (a)–(b) PBDTTPD-HT:ITIC:$PC_{60}BM$ ternary films excited at 560 nm and 710 nm, respectively, and (c) ITIC:$PC_{60}BM$ binary films excited at 710 nm.

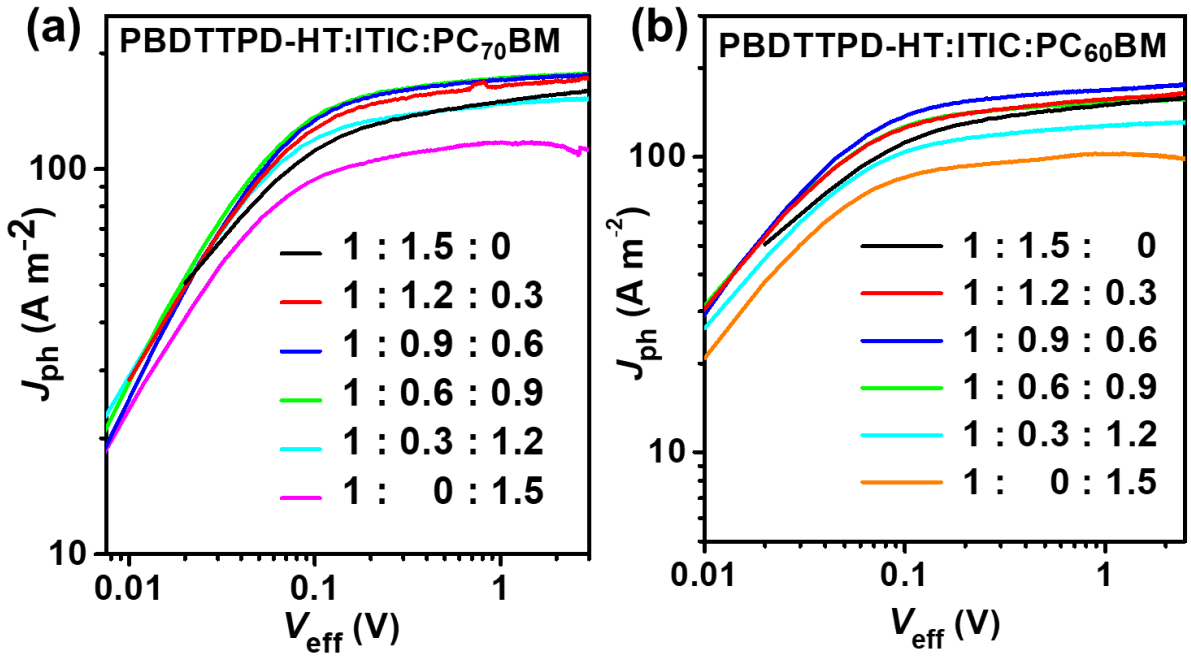

Figure S8. J_{ph}-V_{eff} characteristics of (a) PBDTTPD-HT:ITIC:$PC_{70}BM$ and (b) PBDTTPD-HT:ITIC:$PC_{60}BM$ ternary devices.

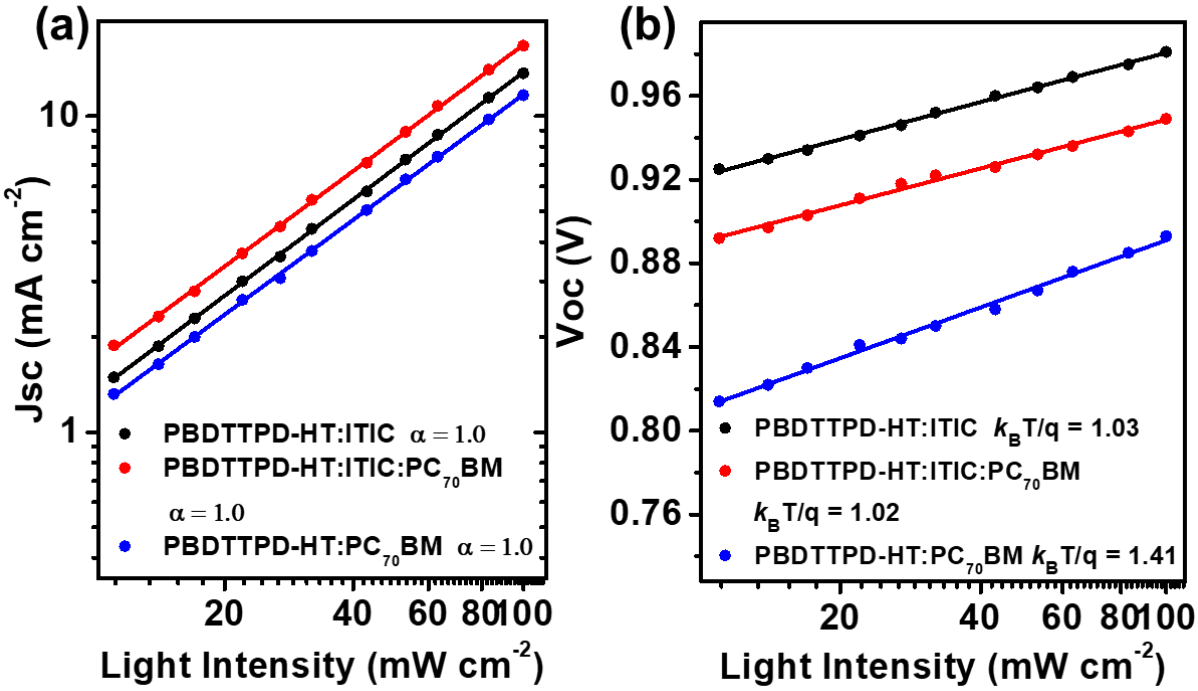

Figure S9. Plots of (a) J_{SC} and (b) V_{OC} vs. light intensity.

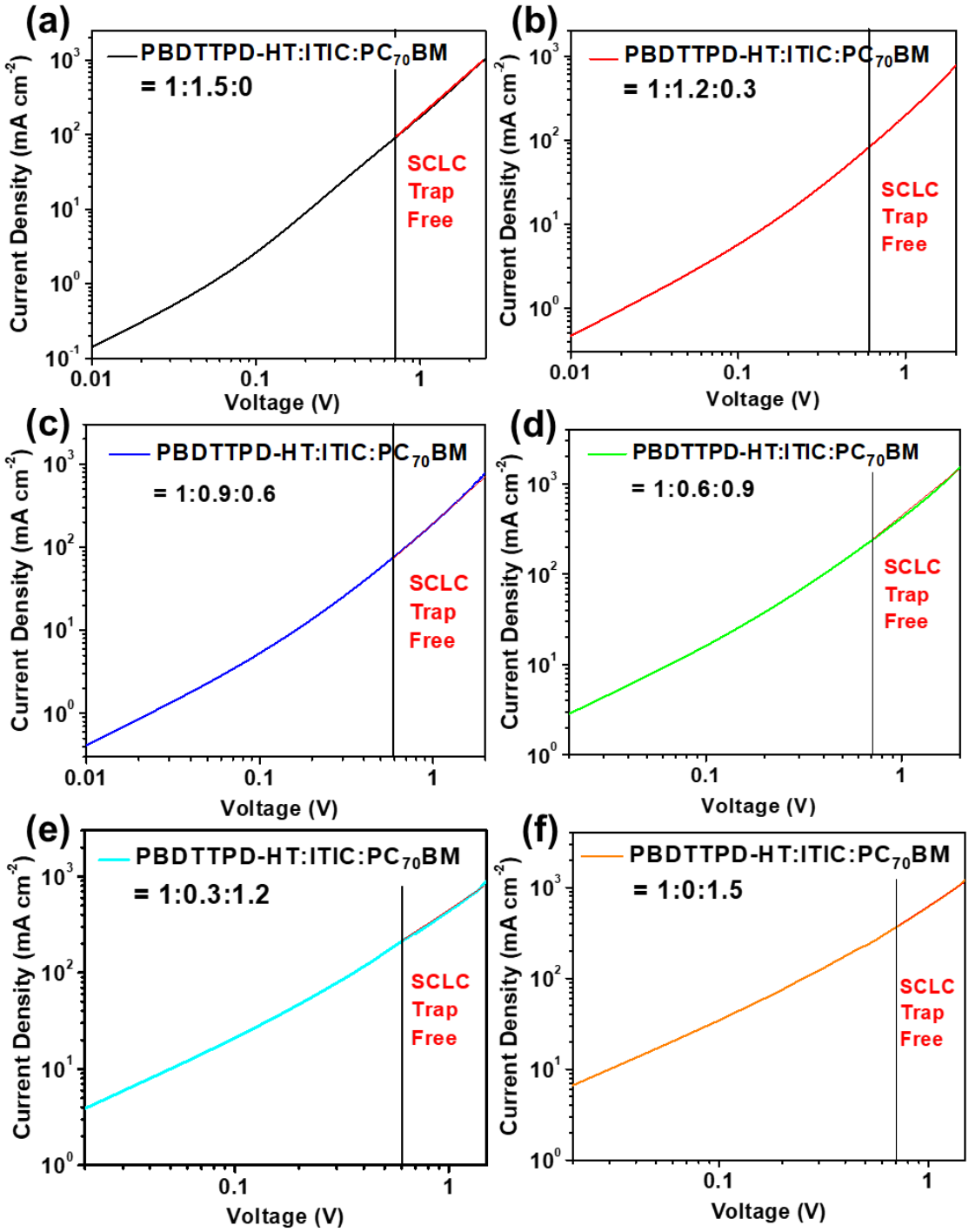

Figure S10. *J-V* characteristics of hole-only devices (ITO/PEDOT:PSS/PBDTTPD-HT:ITIC:$PC_{70}BM$/MoOx/ Ag) with PBDTTPD-HT:ITIC:$PC_{70}BM$ ternary blend films at different weight ratios: (a) 1:1.5:0 w/w, (b) 1:1.2:0.3 w/w, (c) 1:0.9:0.6 w/w, (d) 1:0.6:0.9 w/w, (e) 1:0.3:1.2 w/w, and (f) 1:0:1.5 w/w.

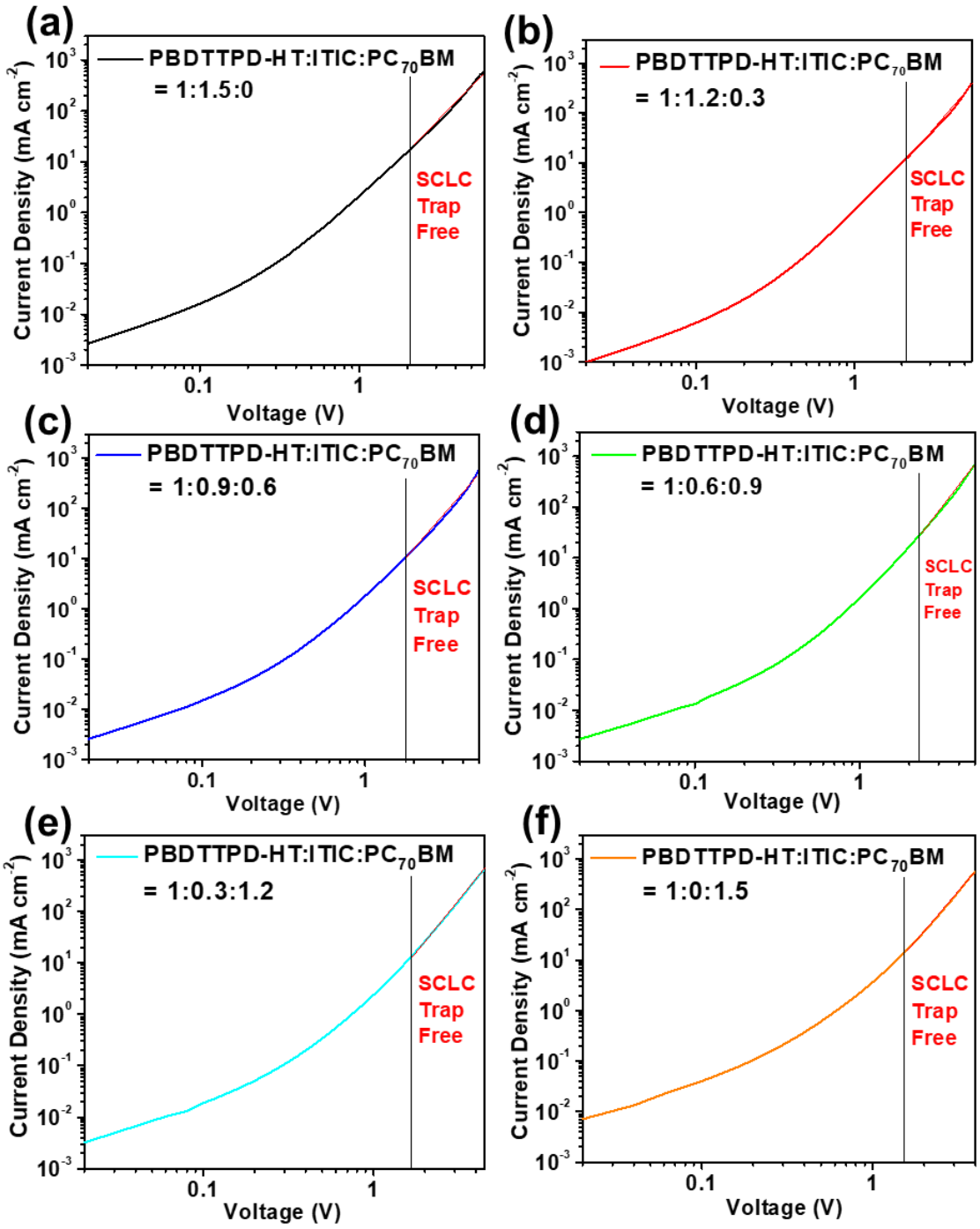

Figure S11. *J-V* characteristics of electron-only devices (ITO/ZnO/PBDTTPD-HT:ITIC:$PC_{70}BM$/ZnO/Ag) with PBDTTPD-HT:ITIC:$PC_{70}BM$ ternary blend films at different weight ratios: (a) 1:1.5:0 w/w, (b) 1:1.2:0.3 w/w, (c) 1:0.9:0.6 w/w, (d) 1:0.6:0.9 w/w, (e) 1:0.3:1.2 w/w, and (f) 1:0:1.5 w/w.

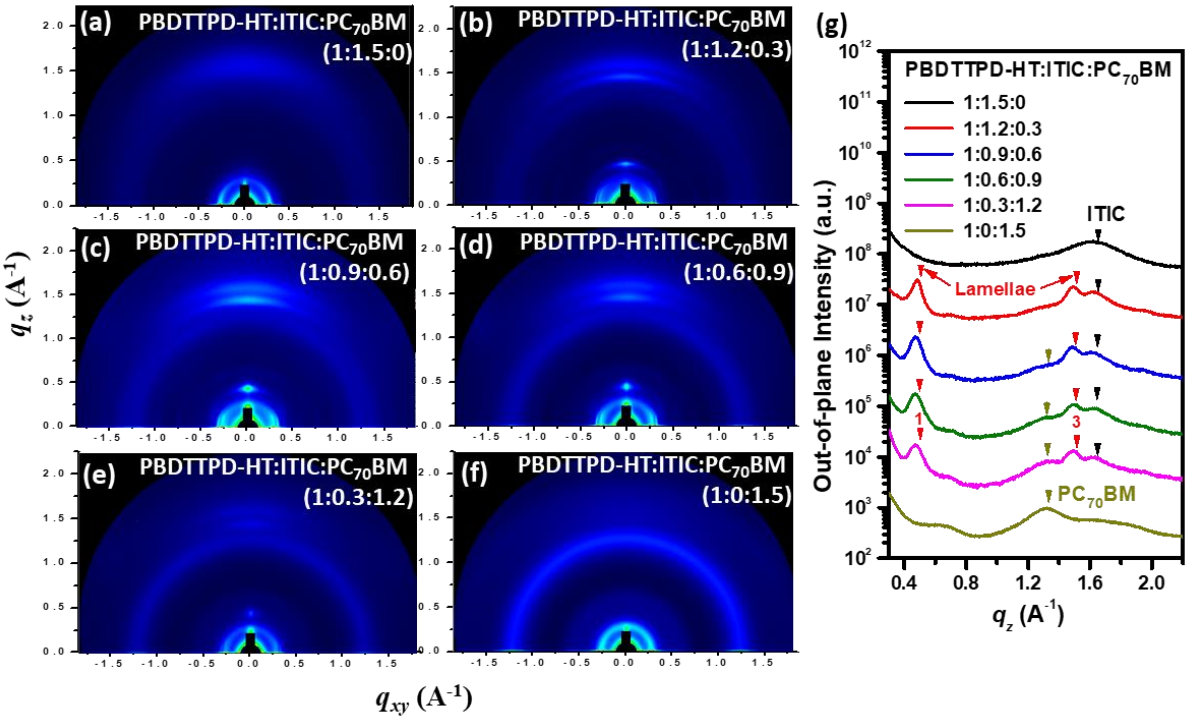

Figure S12. 2D GIWAXS images corresponding to ternary films (PBDTTPD-HT:ITIC:$PC_{70}BM$) of various compositions: (a) 1:1.5:0 w/w, (b) 1:1.2:0.3 w/w, (c) 1:0.9:0.6 w/w, (d) 1:0.6:0.9 w/w, (e) 1:0.3:1.2 w/w, and (f) 1:0:1.5 w/w. (g) Out-of-plane line-cut of corresponding 2D GIWAXS patterns.

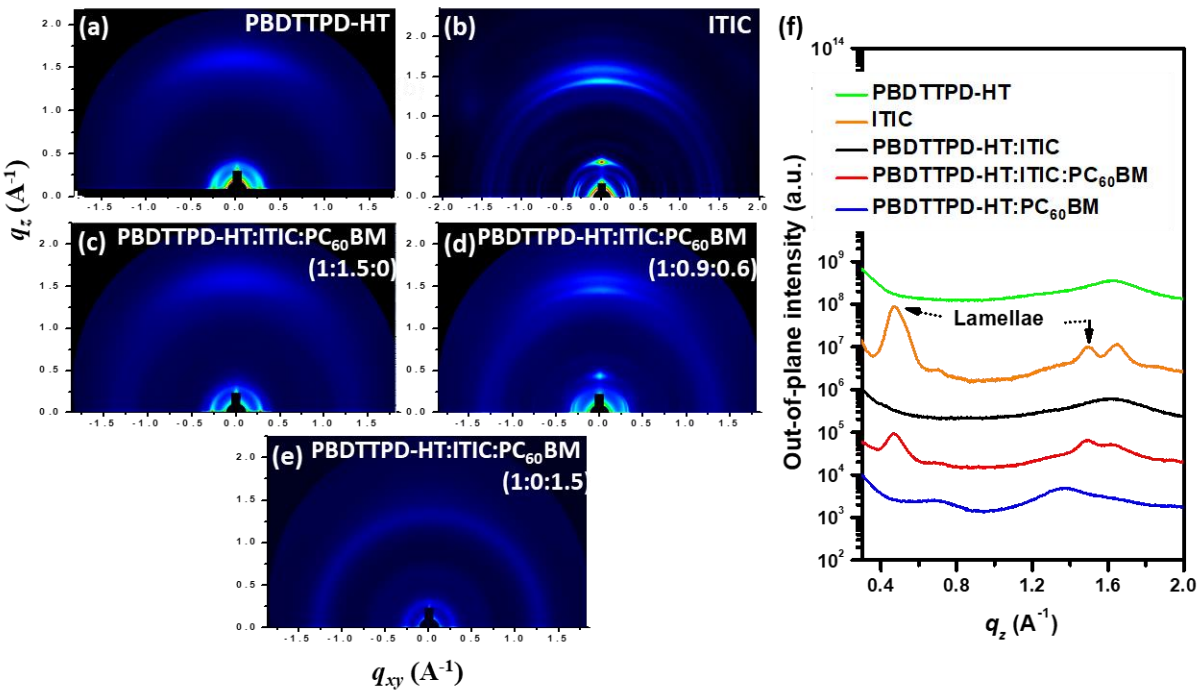

Figure S13. 2- GIWAXS patterns of the pristine (a) D and (b) NFA films, and the PBDTTPD-HT:ITIC:$PC_{60}BM$ films with weight ratio of (c) 1:1.5:0 w/w, (d) 1:0.9:0.6 w/w, and (e) 1:0:1.5 w/w. (f) Out-of-plane line-cut of corresponding 2D GIWAXS patterns.

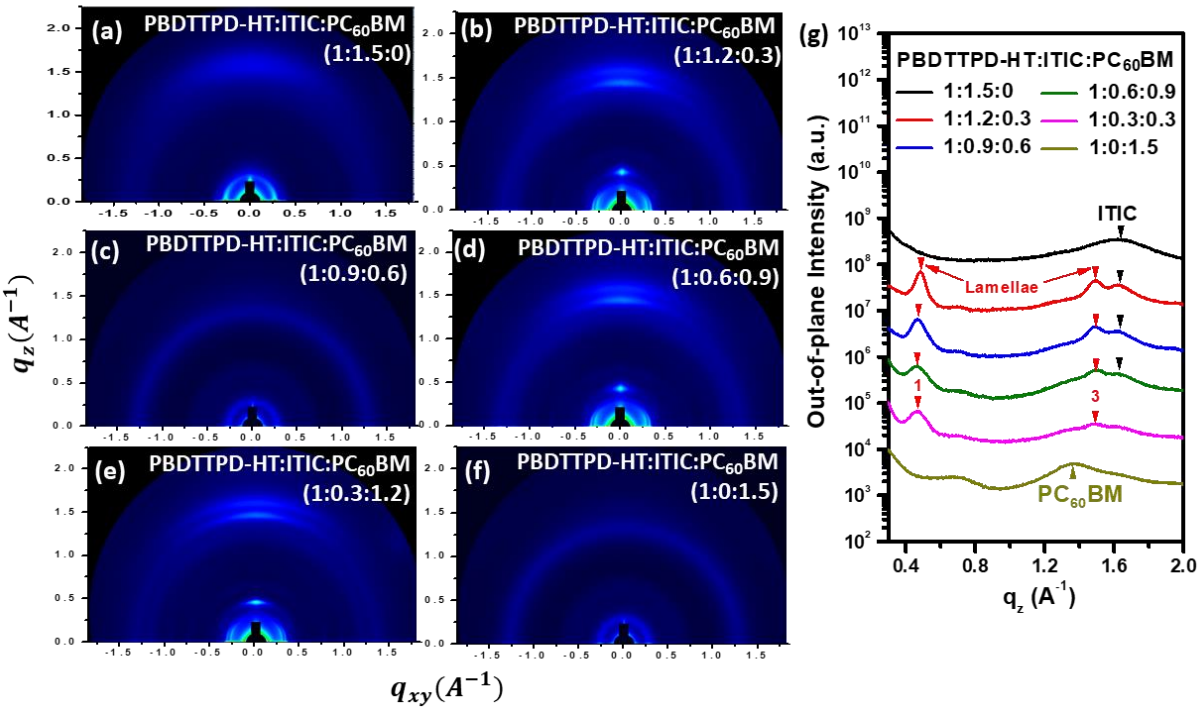

Figure S14. 2D GIWAXS images of the PBDTTPD-HT:ITIC:$PC_{60}BM$ blend films: (a) 1:1.5:0 w/w, (b) 1:1.2:0.3 w/w, (c) 1:0.9:0.6 w/w, (d) 1:0.6:0.9 w/w, (e) 1:0.3:1.2 w/w, and (f) 1:0:1.5 w/w. (g) Out-of-plane line-cut of corresponding 2D GIWAXS patterns.

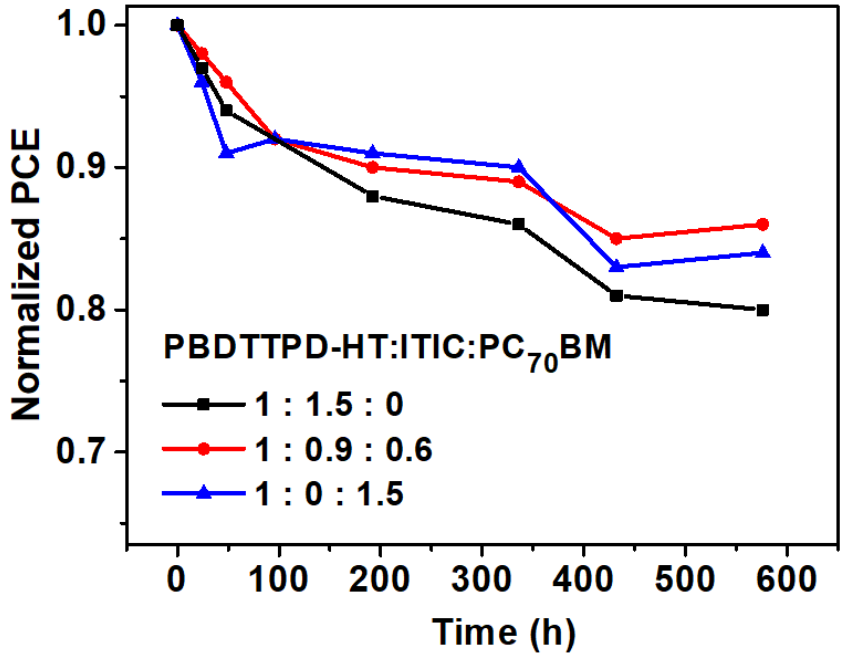

Figure S15. Storage stability of devices. The unencapsulated devices were kept under nitrogen environment and their PCEs were measured occasionally.

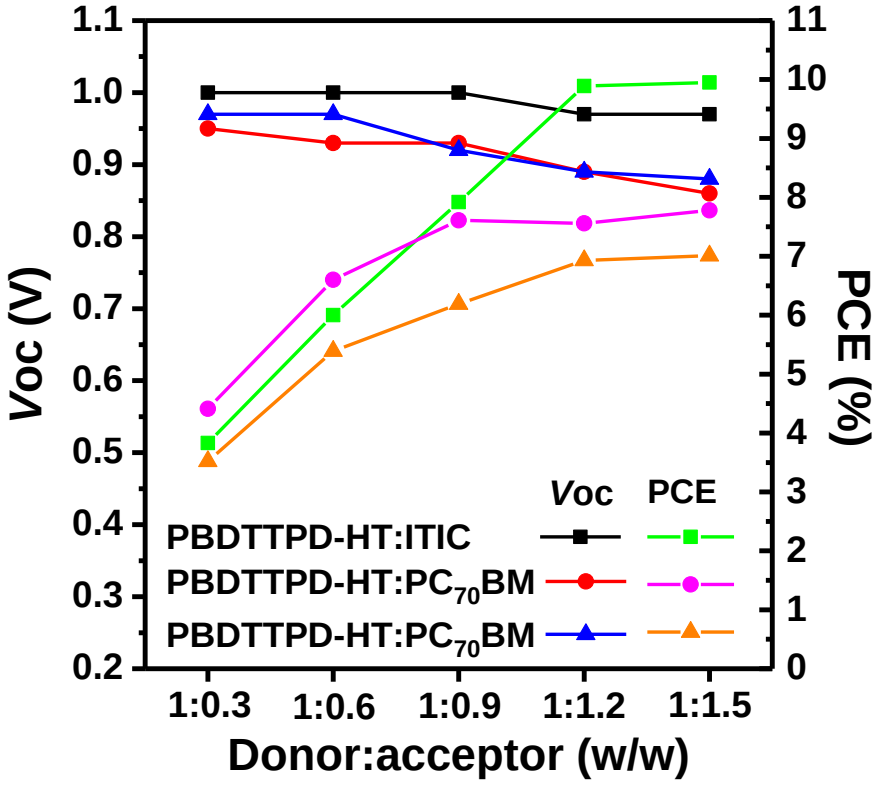

Figure S16. Dependence of V_{OC} and PCE on the donor:acceptor ratio of the binary devices.

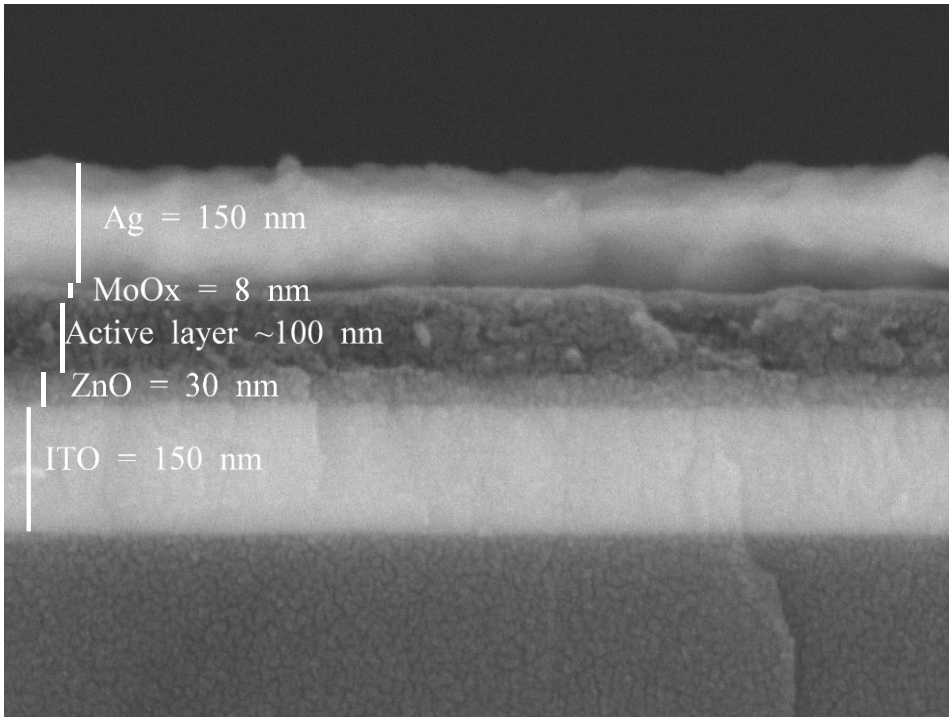

Figure S17. Cross-sectional SEM image of a device.

Table S1. Summary of photovoltaic properties of PBDTTPD-HT:$PC_{70}BM$ binary devices.

PBDTTPD-HT:$PC_{70}BM$	V_{OC} [V]	J_{SC} [mA cm^{-2}]	FF	PCE [%]
1:0.3	0.95	8.66	0.54	4.41
1:0.6	0.93	10.74	0.66	6.60
1:0.9	0.93	11.50	0.71	7.61
1:1.2	0.89	12.06	0.71	7.56
1:1.5	0.86	12.09	0.75	7.78

Table S2. Summary of photovoltaic properties characterizing the PBDTTPD-HT:$PC_{60}BM$ binary devices.

PBDTTPD-HT:$PC_{60}BM$	V_{OC} [V]	J_{SC} [mA cm^{-2}]	FF	PCE [%]
1:0.3	0.97	7.10	0.51	3.52
1:0.6	0.97	9.21	0.61	5.39
1:0.9	0.92	9.74	0.69	6.19
1:1.2	0.89	10.57	0.74	6.93
1:1.5	0.88	10.23	0.77	7.01

Table S3. Summary of photovoltaic properties of PBDTTPD-HT:ITIC binary devices.

PBDTTPD-HT:ITIC	V_{OC} [V]	J_{SC} [mA cm^{-2}]	FF	PCE [%]
1:0.3	1.00	7.26	0.53	3.83
1:0.6	1.00	10.35	0.58	6.00
1:0.9	1.00	12.93	0.61	7.92
1:1.2	0.97	14.80	0.69	9.89
1:1.5	0.97	14.86	0.69	9.95

Table S4. Photovoltaic properties of PBDTTPD-HT:ITIC:$PC_{70}BM$ ternary devices.

PBDTTPD-HT:ITIC:PC_{70}BM	V_{OC} [V]	J_{SC} [mA cm^{-2}]	$J_{calc.}$ [a)] [mA cm^{-2}]	FF	PCE [%] (PCE_{ave})[b)]
1:1.5:0	0.97 (0.97±0.01)	14.86 (14.70±0.39)	14.99	0.69 (0.69±0.01)	9.95 (9.75±0.17)
1:1.2:0.3	0.95 (0.95±0.01)	17.04 (17.06±0.03)	17.03	0.74 (0.72±0.02)	11.89 (11.61±0.23)
1:0.9:0.6	0.95 (0.95±0.01)	17.38 (17.13±0.33)	17.80	0.74 (0.74±0.01)	12.09 (11.86±0.16)
1:0.6:0.9	0.93 (0.93±0.01)	17.04 (16.81±0.39)	16.92	0.74 (0.74±0.01)	11.79 (11.54±0.20)
1:0.3:1.2	0.91 (0.91±0.01)	14.88 (14.79±0.15)	14.56	0.75 (0.74±0.01)	10.07 (9.92±0.08)
1:0:1.5	0.86 (0.86±0.01)	12.09 (11.90±0.14)	11.95	0.75 (0.75±0.01)	7.78 (7.65±0.14)

[a)] J_{SC} calculated from EQE. [b)] The average and standard deviation values in parentheses are obtained from 10 devices.

Table S5. Photovoltaic properties of PBDTTPD-HT:ITIC:$PC_{60}BM$ ternary devices.

PBDTTPD-HT:ITIC:PC_{60}BM	V_{OC} [V]	J_{SC} [mA cm^{-2}]	$J_{calc.}$ [a] [mA cm^{-2}]	FF	PCE [%] (PCE_{ave})[b]
1:1.5:0	0.97 (0.97±0.01)	14.86 (14.70±0.39)	14.99	0.69 (0.69±0.01)	9.95 (9.75±0.17)
1:1.2:0.3	0.96 (0.96±0.01)	16.25 (16.00±0.32)	15.84	0.72 (0.72±0.01)	11.18 (10.90±0.25)
1:0.9:0.6	0.96 (0.95±0.01)	17.17 (16.72±0.39)	17.17	0.73 (0.73±0.01)	11.96 (11.67±0.25)
1:0.6:0.9	0.93 (0.93±0.01)	15.91 (15.67±0.22)	15.60	0.75 (0.75±0.00)	11.17 (11.03±0.17)
1:0.3:1.2	0.92 (0.91±0.01)	13.16 (12.78±0.33)	12.96	0.75 (0.75±0.01)	8.98 (8.69±0.20)
1:0:1.5	0.88 (0.88±0.01)	10.23 (10.22±0.12)	10.13	0.77 (0.75±0.02)	7.01 (6.77±0.24)

[a)] J_{SC} calculated from EQE. [b)] The average values and standard deviations of the device parameters based on at least 10 devices.

Table S6. SCLC mobilities of PBDTTPD-HT:ITIC:$PC_{70}BM$ ternary blend films.

PBDTTPD-HT:ITIC:$PC_{70}BM$	μ_h [$cm^{-2}V^{-1}s^{-1}$]	μ_e [$cm^{-2}V^{-1}s^{-1}$]	μ_h/μ_e
1:1.5:0	7.42×10^{-4}	1.98×10^{-4}	3.75
1:1.2:0	8.32×10^{-4}	2.59×10^{-4}	3.22
1:0.9:0.6	8.59×10^{-4}	2.81×10^{-4}	3.01
1:0.6:0.9	1.54×10^{-3}	3.47×10^{-4}	4.44
1:0.3:1.2	1.35×10^{-3}	4.31×10^{-4}	3.13
1:0:1.5	2.25×10^{-3}	5.43×10^{-4}	4.14